Horizontal variability of near-inertial oscillations associated with the passage of a typhoon

Yukiharu Hisaki
Department of Physics and Earth Sciences, Faculty of Science, University of the Ryukyus, Okinawa, Japan

Tatsunori Naruke
Metocean Environment Inc., Yokohama, Japan

Received 14 October 2002; revised 22 August 2003; accepted 15 October 2003; published 20 December 2003.

[1] Surface currents to the east of Okinawa Island were observed by using HF (high-frequency) ocean radars in August–September 1995. During that period, a typhoon passed near the observation area, and the horizontal variability of near-inertial oscillations associated with the typhoon passage was estimated. In addition, the near-inertial amplitudes and horizontal wave number vectors were estimated. These estimations showed that the near-inertial amplitude was large in the offshore area and small near the coast. The maximum near-inertial wavelength was estimated to be in the order of 1000 km, and the near-inertial wave direction was southward and changed to northwestward on 23 August in 1995. A slab model, incorporating low-frequency currents, was used to calculate near-inertial currents. It was found that the amplitude of calculated near-inertial oscillations was also large in the offshore area. Moreover, the phase-propagation direction of the near-inertial waves was southward and changed to northwestward or westward on 22 August. The growth rate obtained from the dispersion relation was large in the offshore area, where the near-inertial amplitude was large. *INDEX TERMS:* 4572 Oceanography: Physical: Upper ocean processes; 4544 Oceanography: Physical: Internal and inertial waves; 4504 Oceanography: Physical: Air/sea interactions (0312); 4512 Oceanography: Physical: Currents; *KEYWORDS:* inertial current, HF radar, typhoon

Citation: Hisaki, Y., and T. Naruke, Horizontal variability of near-inertial oscillations associated with the passage of a typhoon, *J. Geophys. Res.*, *108*(C12), 3382, doi:10.1029/2002JC001683, 2003.

1. Introduction

[2] Understanding the upper ocean's response to a moving tropical cyclone such as a typhoon or a hurricane has been a major problem for physical oceanography over the past decade [e.g., *Price*, 1981; *Price et al.*, 1994; *Shay et al.*, 1998a; *Zedler et al.*, 2002]. It is possible to conduct observational studies of the ocean response to tropical cyclones only when the tropical cyclone passes near an observation system. Okinawa Island is located to the southwest of mainland Japan, and typhoons often pass near the island. The current field near the Okinawa Island is affected by the Kuroshio current in the East China Sea and mesoscale eddies.

[3] The surface current field to the east of Okinawa Island was described by *Hisaki et al.* [2001] according to observation by HF (high-frequency) ocean radars in the spring of 1998. Prior to their observation by HF ocean radars in 1998, we observed ocean currents by HF ocean radars from August 1995 to September 1995. During the observation period, Typhoon 9507 (Janis) passed by the observation area. The surface current associated with the passage of that typhoon is described in the current study.

[4] Near-inertial oscillations are often observed in the upper ocean, especially when the surface wind stress changes with the passage of a storm. The horizontal variability of near-inertial oscillations varies with wind-forcing, location, and geostrophic shear. For example, although they investigated the non-hurricane forced case, *Chen et al.* [1996] showed that near-inertial oscillations were the largest in the shelf break, decaying gradually toward the coast but then decreasing rapidly offshore. The near-inertial currents also interact with mesoscale eddies. There are theoretical studies on the relation between near-inertial oscillations and geostrophic shear [e.g., *Weller*, 1982; *Kunze*, 1985; *van Meurs*, 1998; *Young and Ben Jelloul*, 1997]. *Kunze* [1985] derived a dispersion relation of the near-inertial waves under the WKB approximation; that is, near-inertial wave scales are much smaller than the flow scale.

[5] *van Meurs* [1998] showed that the gradients in the mesoscale vorticity are important for factors in the evolution of the near-inertial mixed-layer currents when the spatial scales of the near-inertial and geostrophic currents are similar. These studies, in turn, suggest that if the vorticity scales of the

0148-0227/03/2002JC001683$09.00

quasi-geostrophic ocean features are considerably less than the near-inertial wave scale, the quasi-geostrophic current field may not necessarily play a significant role in the near-inertial wave evolution.

[6] On the other hand, *Young and Ben Jelloul* [1997] show that mesoscale eddies do affect the evolution of near-inertial waves. The prediction of the inertial wave field by considering its interaction with mesoscale eddies is insufficient. For example, *D'Asaro* [1995] noted that mesoscale circulation was not resolved in the Ocean Storms Experiment; therefore, they could not account for the interaction between those eddies and the inertial wave field. It is necessary to observe currents at a fine spatial resolution in order to investigate the interaction between inertial currents and mesoscale (low-frequency) currents.

[7] HF ocean radars can measure ocean currents at a fine resolution. An HF ocean radar system has been shown to be one of the most promising methods of effectively measuring a spatially evolving current [*Takeoka et al.*, 1995; *Hisaki et al.*, 2001] and wave fields [*Hisaki*, 1996, 2002, 2003]. There have been several studies using HF ocean radars at a fine resolution to investigate the horizontal variability of near-inertial currents [*Shay et al.*, 1998b; *Chant*, 2001; *Peters et al.*, 2002]. These previous studies showed that the near-inertial current is highly variable even in the HF radar observation domain (about 50 km square). However, the observation area of these studies was a continental shelf; that is, the water depth of the observation area was less than about 200 m in the study by *Shay et al.* [1998b] and *Peters et al.* [2002], and less than about 25 m in the study by *Chant* [2001].

[8] On the other hand, the water depth of our observation area ranges from 200 m to 2000 m. The difference of horizontal currents between shallow and deep areas can therefore be investigated from our observation. The surface currents in the area deeper than about 1000 m were affected by mesoscale eddies, while winds affected surface currents in the region shallower than about 1000 m [*Hisaki et al.*, 2001]. The objective of the current study is to investigate the horizontal variability of near-inertial oscillations in an observation area characterized by deep and coastal areas.

[9] In section 2, we describe the experimental design and general features of typhoon (tropical storm) Janis. Section 3 presents the observation by HF ocean radars. The horizontal variability of near-inertial currents was investigated based on the simple slab model in section 4. The result is discussed in section 5. Section 6 presents conclusions. Vertical properties of near-inertial oscillations were not investigated.

2. Observation

2.1. Experimental Design and Data Analysis

[10] The HF ocean radars of the Okinawa Radio Observatory (Okinawa Subtropical Environment Remote-Sensing Center), Communications Research Laboratory, were deployed along the east coast of Okinawa Island (Figure 1). The inertial period (*IP*) is about 27 hours.

[11] The radars were located at site A (26°04′48″N, 127°41′23″E) and site B (26°16′55″N, 127°48′26″E) in Figure 1. The radio frequency was 24.515 MHz, and the temporal resolution of the radar system is 2 hours. The measured current vectors were mapped onto a grid with a horizontal resolution of 1.5 km as shown in Figure 1. The radar is a beam-forming type, and the beam forming is electronically controlled by the phase shifter in real time. The details of the radar system are described by *Hisaki et al.* [2001].

[12] The observation period for the HF ocean radars was from 2 August 1995 to 10 September 1995. However, the data were actually recorded from 15 August to 17 August and from 20 August to 10 September. The HF-ocean-radar-derived currents were compared with the currents measured by the current meter described by *Hisaki et al.* [2001]. The correlations were greater than 0.85, and the root-mean square difference between the sensors was about 10 cm s^{-1} [*Hisaki et al.*, 2001]. The HF ocean radar-derived currents can thus be considered sufficiently accurate for our purposes.

[13] The surface wind data at 10-min intervals at the location Itokazu (I, 26°09′N, 127°46′E, elevation: 186 m) were supplied by the Japan Meteorological Agency (JMA). The wind field for Typhoon Janis is not accurately known. We used two sets of the best track data of the typhoon from JMA and the U.S. Joint Typhoon Warning Center (JTWC) [*Etro and Bassi*, 1995] located at Guam.

[14] There were some differences between the two data sets. The JMA best track data included the position of the storm center (latitude and longitude), central pressure (p_c), maximum wind speed (U_{max}), and the radius of 15 m/s wind speeds (R_{15}). The central pressure and maximum wind speed were inferred from the method of *Dvorak* [1975], and the value of R_{15} was inferred from the method of *Hagiwara et al.* [1989].

[15] Hourly sea level pressure data at JMA stations were also used in order to construct a tropical-cyclone wind-profile model (TCWPM). The JMA stations are Naze (Nz, 28°22.6N, 129°29.9E), Yonaguni (Yg, 24°27.7N, 123°0.6E), Ishigaki (Is, 24°19.9N, 124°9.8E), Miyako (Mk, 24°47.4N, 125°16.7E), Kume (Km, 26°20.1N, 126°48.3E) Naha (Nh, 26°12.2N, 127°41.3E), Nago (Ng, 26°35.4N, 127°58.1E), Okinoerabu (Ok, 27°25.7N, 128°42.4E), and Minami-Daito (Md, 25°49.7N, 131°13.5E). The three-hourly sea level pressure and sea-surface winds were observed by a JMA buoy (28°10'N, 126°20′E). The center pressure data of the typhoon estimated by JMA were also used to construct the TCWPM.

2.2. Pressure and Wind Models

[16] The TCWPM was used to infer the parameters of typhoon Janis and to investigate the effect of horizontal variability of winds on near-inertial currents. Sea level pressure p at position vector $\mathbf{r}$ relative to the storm center is expressed by Schloemer's model as

$$p = p_c + (p_n - p_c)\exp\left(-\frac{r_0}{r}\right), \tag{1}$$

where $r = |\mathbf{r}|$ is the horizontal distance to the storm center, and p_n is the ambient pressure, which is evaluated from the JMA weather chart. A typical value of p_n is 1010 hPa. If the Coriolis force is small in comparison to the pressure gradient and centrifugal force, the air will be in cyclostric balance. Parameter r_0 is the radius of the maximum gradient winds [*Holland*, 1980]. It is estimated from the JMA pressure

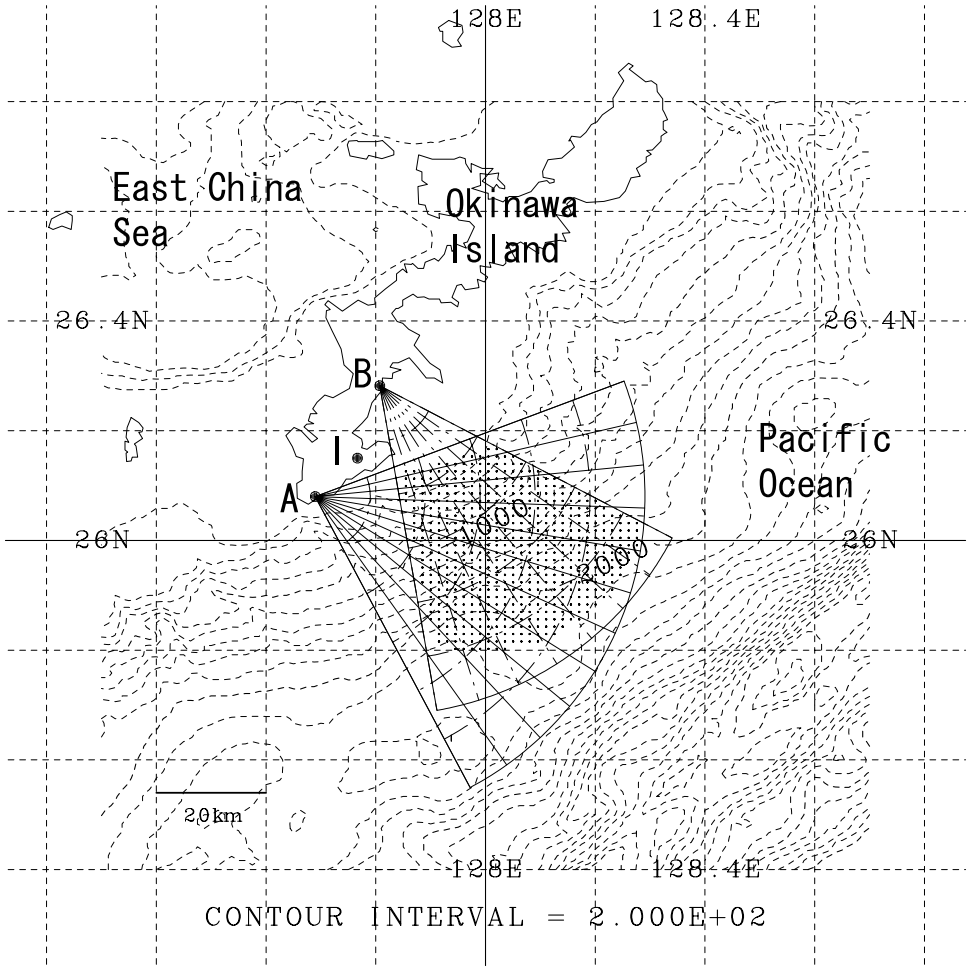

Figure 1. Map of the observation area.

data and JMA best track data as described in section 2.1. The storm transition vectors ($\mathbf{U}_t$) are estimated from JMA best track data. Gradient wind speed V_g is written as

$$V_g = \frac{1}{2} rf \left[-1 + \left(1 + \frac{4}{\rho_a r f^2} \frac{\partial p}{\partial r} \right)^{1/2} \right], \tag{2}$$

where ρ_a is air density, and f is the Coriolis parameter. Equations (1) and (2) may accurately model the radial dependence of tropical cyclone tangential winds in the inner core region, but they do not accurately model the outer wind structure of a tropical cyclone since equation (2) extends the cyclonic winds to infinity [*Carr and Elsberry*, 1997]. Equation (2) was used to infer the radius of maximum winds, R_{max}.

[17] The Carr and Elsberry model was used [*Carr and Elsberry*, 1997; *Chu et al.*, 2000] to compute the wind vector relative to the center of the tropical cyclone ($\mathbf{V}_c(r) = (v_t, v_r)$) as

$$v_t(r) = \frac{f_0}{2} \left[R_0 \left(\frac{R_0}{r} \right)^{2/5} - r \right] \frac{a^4}{1 + a^4} \tag{3}$$

$$v_r(r) = v_t \tan \gamma, \tag{4}$$

where R_0 is the radii of zero tangential velocities, v_t and v_r are the radial and tangential velocity components, γ is the inflow angle of the wind, $f_0 = f$ at the storm center, and $a = r/R_{max}$. Note that $|\mathbf{V}_c(r)| = 0$ for $r > R_0$. The parameter R_0 is estimated from the equation $|\mathbf{V}_c(R_{15})| = 15$ for a given γ. The wind vector of TCWPM ($\mathbf{V}_{TC}$) is expressed by the combination of the wind vector relative to the center of the tropical cyclone ($\mathbf{V}_c$) and the storm transition vector ($\mathbf{U}_t$) expressed as

$$\mathbf{V}_{TC} = \frac{1}{1 + c^4} (\mathbf{V}_c + \mathbf{U}_t), \tag{5}$$

where $c = r/(0.9R_0)$ [*Chu et al.*, 2000]. Optimal inflow angle γ is estimated by comparing the wind vectors of the TCWPM (equation (5)) with observed sea surface winds at a JMA buoy, and $\gamma = 0$. The RMS difference between wind speeds of TCWPM and sea-surface wind speeds at the JMA buoy was 1.76 m/s when the distance between the storm center and the JMA buoy was less than 350 km.

2.3. Typhoon Janis

[18] Typhoon (tropical storm) Janis initially formed as a tropical disturbance around (12°N, 144°E) on 17 August 1995. After formation, this tropical disturbance moved

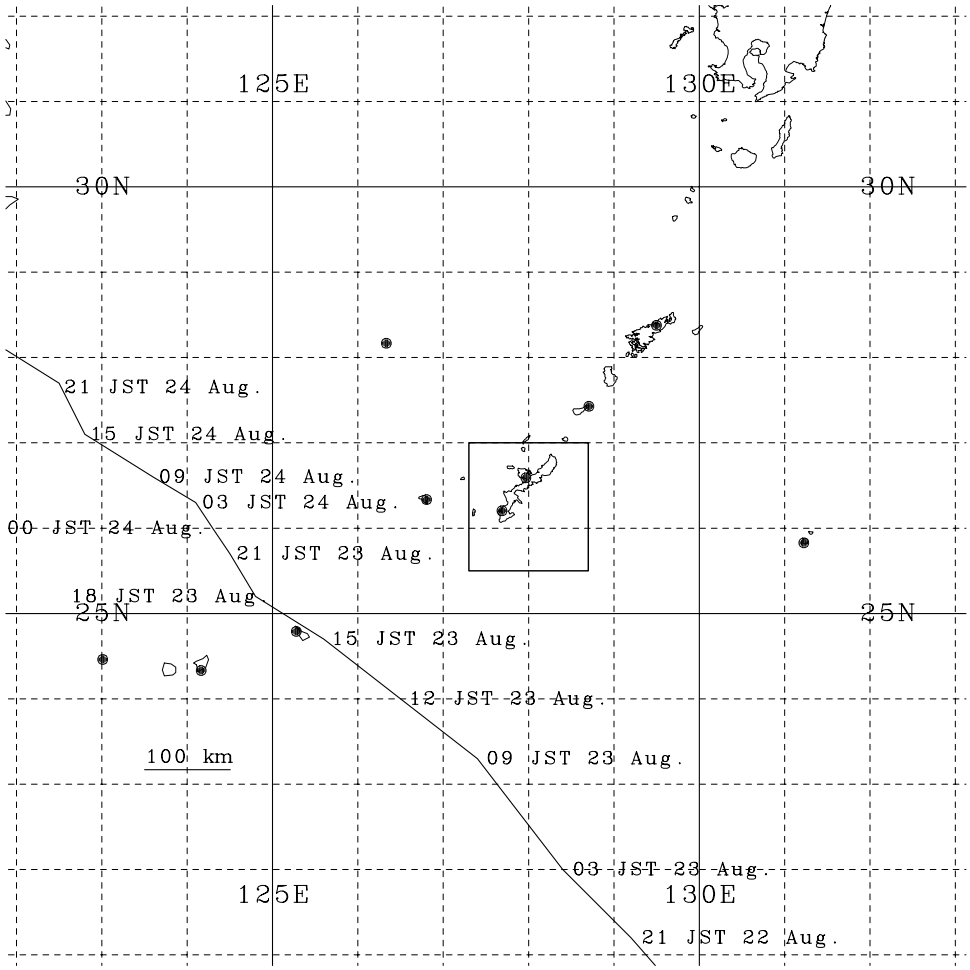

Figure 2. Track of typhoon Janis. The solid circles are locations of JMA stations and a JMA buoy (section 2.1). The box (127.3°E to 128.7°E and 25.5°N to 27.0°N) outlines the area of Figure 1 for reference.

northwestward and slowly became more organized [*Etro and Bassi*, 1995].

[19] Figure 2 indicates the track of the typhoon Janis in the vicinity of the Okinawa Island from JMA data. The HF-radar observation area was located to the right side of the center of the typhoon. Rightward bias, which is the enhancement of the inertial oscillation to the right of the storm path due to the clockwise rotation of both wind vectors and inertial currents in time [*Price*, 1981], may occur in the HF-radar observation area.

[20] The closest distance between the HF-ocean-radar observation area and the center of the typhoon was about 260 km at 1200 local time (LT) 23 August. From JMA data, the minimum surface pressure was 990 hPa, and the maximum wind speed was 23 m/s (45 knots) at 2100 LT 24 August. On the other hand, from JTWC data, the maximum wind speed was 28 m/s (55 knots) at 2100 LT 24 August. The gale radius was about 200 km.

[21] Figure 3 shows a time series of hourly wind vectors at Itokazu (I in Figure 1) from 18 August to 28 August 1995. The wind direction was northwestward until 20 August. On 20 August, the wind vectors rotated counterclockwise and changed to the southwestward direction. The wind direction was northwestward from 0600 LT to 1000 LT 21 August, but the direction changed to southwestward. It then changed to northwestward again at 1100 LT 21 August, and wind speed increased. The wind speed was greater than 10 m/s from 1900 LT 22 August to 0900 LT 24 August. The maximum hourly wind speed in Itokazu was 14.5 m/s at 1400 LT 23 August.

2.4. Typhoon Parameters and Structure

[22] Table 1 lists the parameters of typhoon Janis as it passed near the HF-ocean-radar observation area. Most

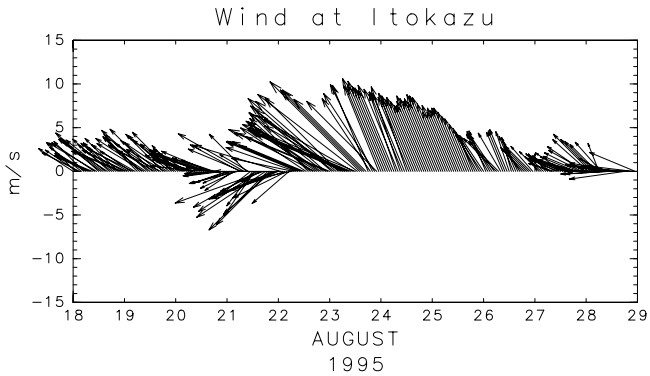

Figure 3. Time series of hourly winds at Itokazu ("I" in Figure 1).

Table 1. Parameters of Typhoon Janis

Time (LT) and Date	r_0, km	p_c, hPa	U_t, m/s	R_{max}, km	U_{max}, m/s	$IP \times U_t$, km
0300 23 August	102	998	7	81	21	794
0900 23 August	90	998	10	73	18	1045
1500 23 August	108	998	10	83	18	1038
2100 23 August	95	996	5	77	20	470
0300 24 August	84	996	3	69	20	303
0900 24 August	48	994	4	43	20	349

parameters were obtained from JMA best-track data. Parameter R_{max} (radii of maximum wind speed) was estimated by seeking the maximum of equation (2). The transition speed $U_t = |\mathbf{U}_t|$ is large, when the typhoon is close to the HF-ocean-radar observation area. The parameter $IP \times U_t$, which is proportional to the oceanic wavelength of the response induced by a moving tropical cyclone [*Price*, 1983], was large on 23 August. The values of r_0 and R_{max} become smaller when the typhoon intensity becomes larger.

[23] Figure 4 shows examples of pressure field, wind speed, wind stress curl, and wind stress divergence. The wind stress was calculated from the bulk formula of *Large and Pond* [1981]. The pressure field is symmetric with respect to the storm center. It can be seen that the wind speed field is asymmetric (Figure 4b), because of the storm motion. The distance between HF-ocean-radar observation area and the storm center is about 3 times R_{max} at 1500 LT 23 August.

[24] The wind stress field curl is negative in most of the observation area. The stress-divergent field is convergent in front of the storm (Figure 4d). We can expect that the wind stress field is convergent before the typhoon passage, and the wind stress field is divergent after the typhoon passage.

2.5. Mesoscale Eddies

[25] Figure 5 presents maps of sea level anomalies (SLA) in the region east of Okinawa Island during the observation period of the HF ocean radars. The SLA were estimated from altimetric data by ERS and TOPEX/Poseidon, and provided from Archiving, Validation and Interpretation of Satellite Oceanographic data (AVISO). The SLA from AVISO altimetric data were estimated by removing the time-mean surface from 1993 to 1995, geoid heights, tidal height signals, and the effects of the inverse barometer [*AVISO*, 1998].

[26] An anticyclonic eddy can be seen in the vicinity of the HF radar observation area. The mean geostrophic currents are weak compared to geostrophic current anomalies in this region [e.g., *Hisaki et al.*, 2001]; therefore, we can expect northeastward geostrophic currents in the HF-radar observation area.

3. Surface Currents Observed by HF Radar

[27] Figure 6 shows examples of surface currents observed by HF ocean radars the passage of typhoon Janis (Figure 6a) and a non-typhoon period (Figure 6b). The surface currents are mainly composed of geostrophic currents, wind-driven currents, and high-frequency currents such as tidal and near-inertial currents. In the typhoon period, the HF-radar observation area was small, because the SN (signal to noise) ratio in the measured Doppler spectra was low in the high-sea state because of the loss of radio waves in the propagating sea surface.

[28] The surface currents in the offshore region were northeastward in both Figures 6a and 6b. The currents were associated with the anticyclonic eddy shown in Figure 5.

[29] Geostrophic currents also contribute to surface currents in the offshore region even during the typhoon period. The surface currents in the nearshore region in Figure 6a were northwestward, because wind-driven currents were dominant in the observed surface currents. The wind-driven current was likely to be dominant in the nearshore region, while currents associated with the eddy contribute to observed surface currents in the offshore area as suggested by *Hisaki et al.* [2001].

[30] The background current field, which is inferred as geostrophic currents from density profiles, should be removed to examine the kinematical response to the strong forcing [*Shay et al.*, 1998a]. However, because we do not have density profiles, only low-frequency currents were estimated as a background current. The estimated low-frequency current may include the geostrophic current associated with the horizontal density gradients induced by the typhoon.

[31] The low-frequency current vectors were estimated by the following method. Because there were data gaps, as shown in Figure 6a, we estimated low-frequency currents by fitting sine waves plus a linear trend to the observed currents by the least squares method. The periods of the sine waves were $T_p = 384/i$ (hour) ($i = 1, .., N_p$, $N_p = 8$), and four main tidal periods (M_2: 12.42 hour, K_1: 23.93 hour, S_2: 12.0 hour, O_1: 25.82 hour). The harmonic constants were also estimated by this method, and the currents were detided by using the four main tidal coefficients.

[32] Figure 7 shows examples of low-frequency currents, (relative) vorticity, and horizontal divergence of the currents. The vorticity and divergence were normalized by local inertial frequency f. The current directions were northeastward. The magnitudes of the low-frequency currents were small near the coast but large in the offshore area. As a result, the vorticity of the low-frequency currents was positive in most of the observation area, although an anticyclonic eddy can be seen in Figure 5. The relative vorticity was negative only in the southeastern part of the observation area. These features can be seen in both Figures 7b and 7e. The negative vorticity area was the largest in Figure 7e and the smallest in Figure 7h in this example. In Figure 7c, the divergence was positive south of latitude 26°N, which is associated with the transition between negative and positive vorticity areas. The low-frequency current was convergent in the eastern part of the observation area at 1200 LT 23 August (Figure 7f). The magnitude of the divergence was smaller than that of the vorticity. The positive or negative divergent areas were variable with time (Figures 7c, 7f, and 7i).

[33] The authors expected that near-inertial currents associated with the passage of the typhoon would be dominant during the observation period. Figure 8 shows rotary spectra of raw and detided currents at a nearshore point (26.059°N, 127.945°E) and an offshore point (25.951°N, 128.065°E). The rotary spectra are estimated by MEM (Maximum Entropy Method), and the order of the autoregressive model was estimated by the Burg method. The period of the spectral analysis is from 1400 LT

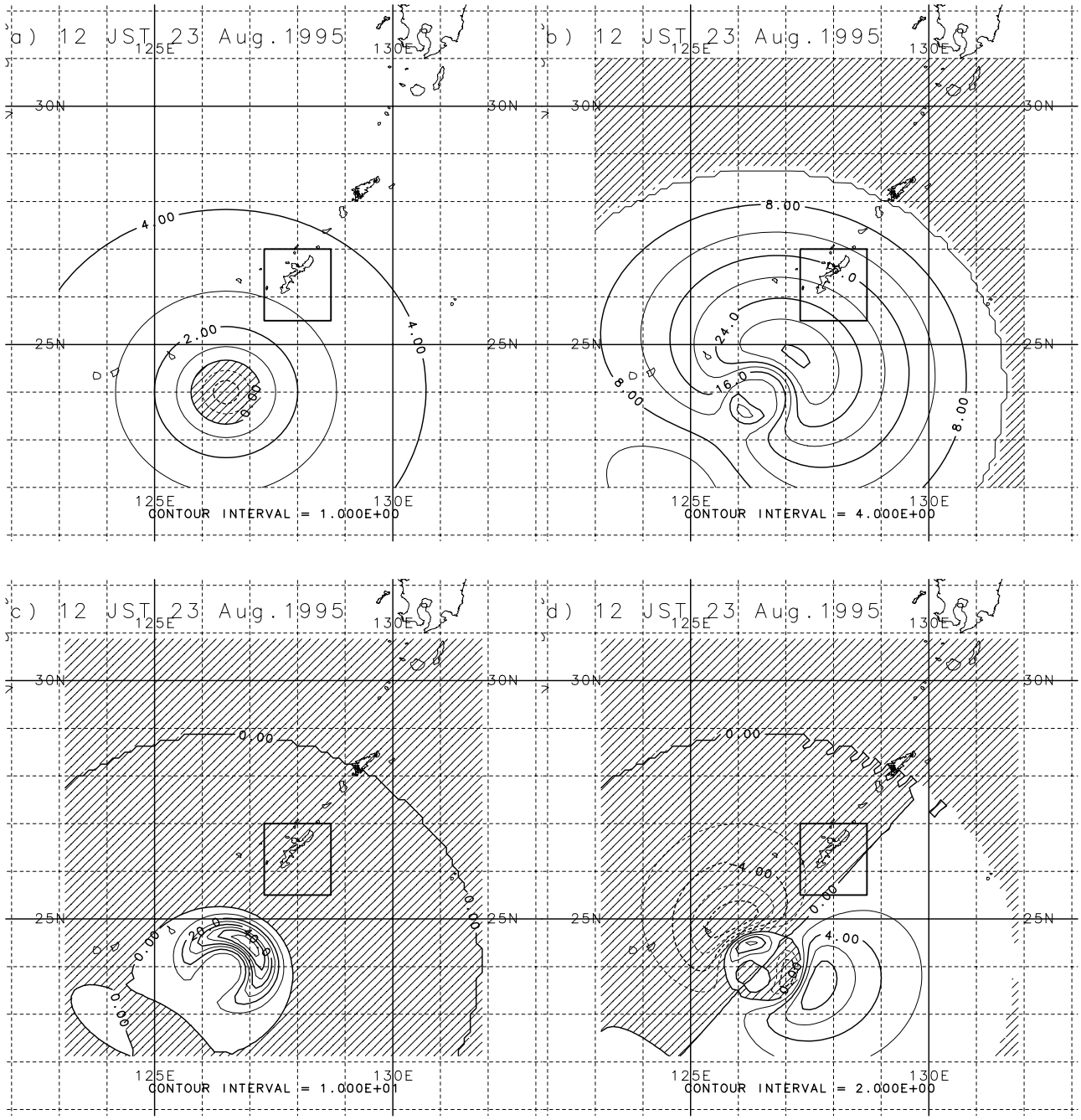

Figure 4. Example of the horizontal structure of typhoon Janis described by equations (5) and (1) at 1500 LT (here JST) 23 August 1995. The hatched areas indicate negative values. (a) Sea level pressure-1000 (unit: hPa; contour interval: 1 hPa), (b) wind speed (unit: m/s; contour interval: 4 m/s, (c) wind stress curl (unit: 10^{-6} N/m^3; contour interval: 10^{-5} N/m^3), and (d) wind stress divergence (unit: 10^{-6} N/m^3; contour interval: 2×10^{-6} N/m^3). The box in each panel (127.3°E to 128.7°E and 25.5°N to 27.0°N) outlines the area of Figure 1 for reference.

20 August 1995 to 2200 LT 10 September 1995. Spectra of raw currents are also shown in order to compare with the spectra of the detided currents. It is clear that near-inertial currents with clockwise rotation are dominant in Figure 8.

[34] Furthermore, the spectral level at the inertial frequency at the offshore point is larger than that in the nearshore area. The peak frequency of the detided currents is equal to the inertial frequency in Figure 8b. It is different from the inertial frequency in Figure 8b. This result may have nothing to do with the subinertial current-vorticity field due to the mismatch in scales.

[35] The spectra is flat above a 12-hour semidiurnal tide except the peaks at 6 and 8 hours. These peaks may be side lobes or compound tides. The sampling interval of HF ocean radar currents was 2 hours, and the band higher than 10 hours is defined only by less than five data points. The

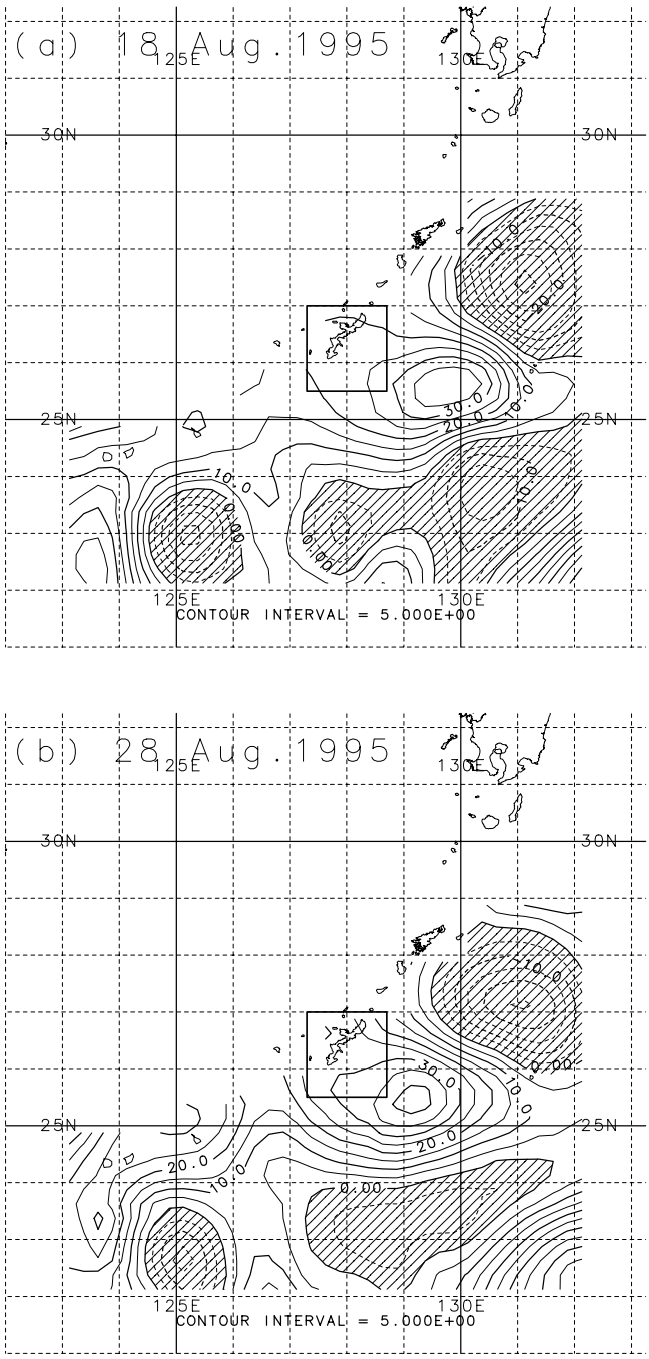

Figure 5. Maps of spatial distributions of SLA (sea level anomalies) during the HF-ocean-radar observation period: (a) 18 August 1998; (b) 28 August 1998; units: cm; contour interval: 5 cm. The box in each panel (127.3°E to 128.7°E and 25.5°N to 27.0°N) outlines the area of Figure 1 for reference.

flat shape of the spectra was due to noise according to *Shay et al.* [1995, 1998c], while their sampling interval of HF ocean radar currents was 20 min.

[36] We examined the temporal and spatial changes in energy distributed near the inertial frequency by the complex demodulation, which is similar to that of *Brink* [1989] and *Emery and Thompson* [1998]. The method was to estimate a near-inertial amplitude A and a phase ϕ by seeking the minimum of I defined as

$$I = \sum_{l=-L}^{L} |u(t_l) + iv(t_l) - A\exp(-iFt_l - i\phi) - at_l - b|^2, \quad (6)$$

where $t_l = t + l\Delta t$, $(u(t), v(t))$ is the detided currents at time t, and Δt = 2 hours. The real variables A (amplitude), ϕ (phase), a (slope), and b (bias) at time t were estimated by the least squares method. The parameter L = 14 and the

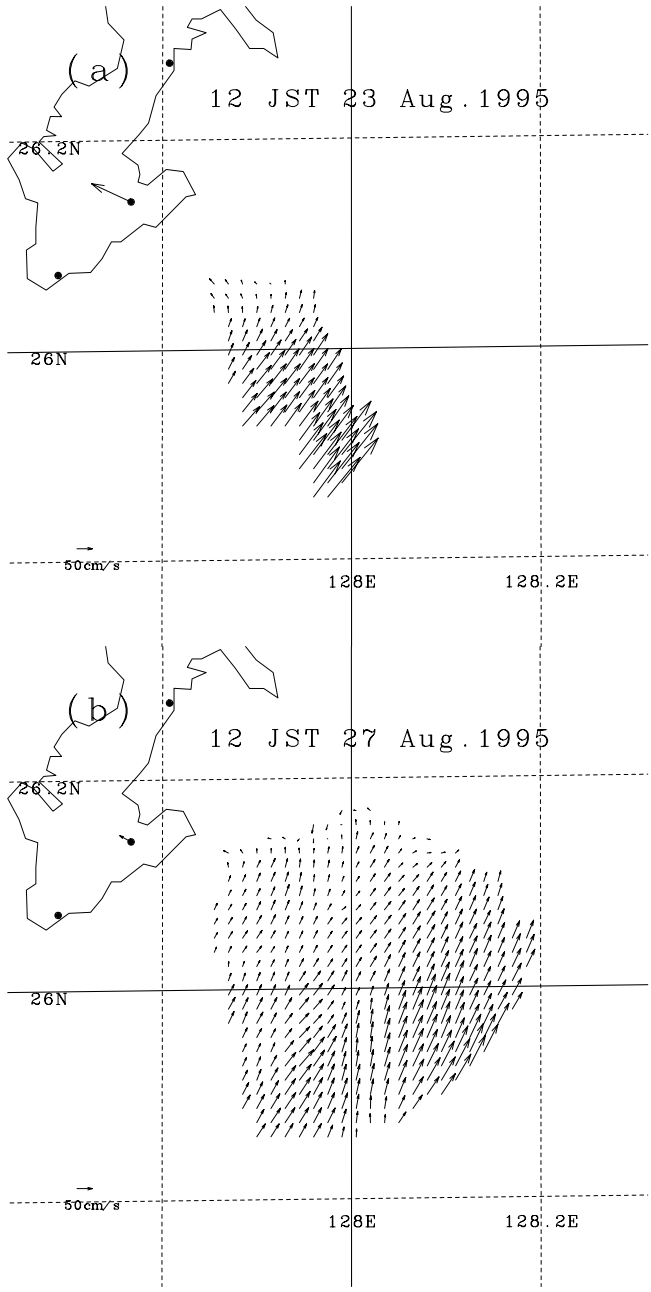

Figure 6. Surface currents observed by HF ocean radars in (a) the typhoon period (1200 LT 24 August 1995) and the (b) non-typhoon period (1200 LT 27 August 1995). The arrow at I (Figure 1) is the wind vector at the time (10% of the magnitude).

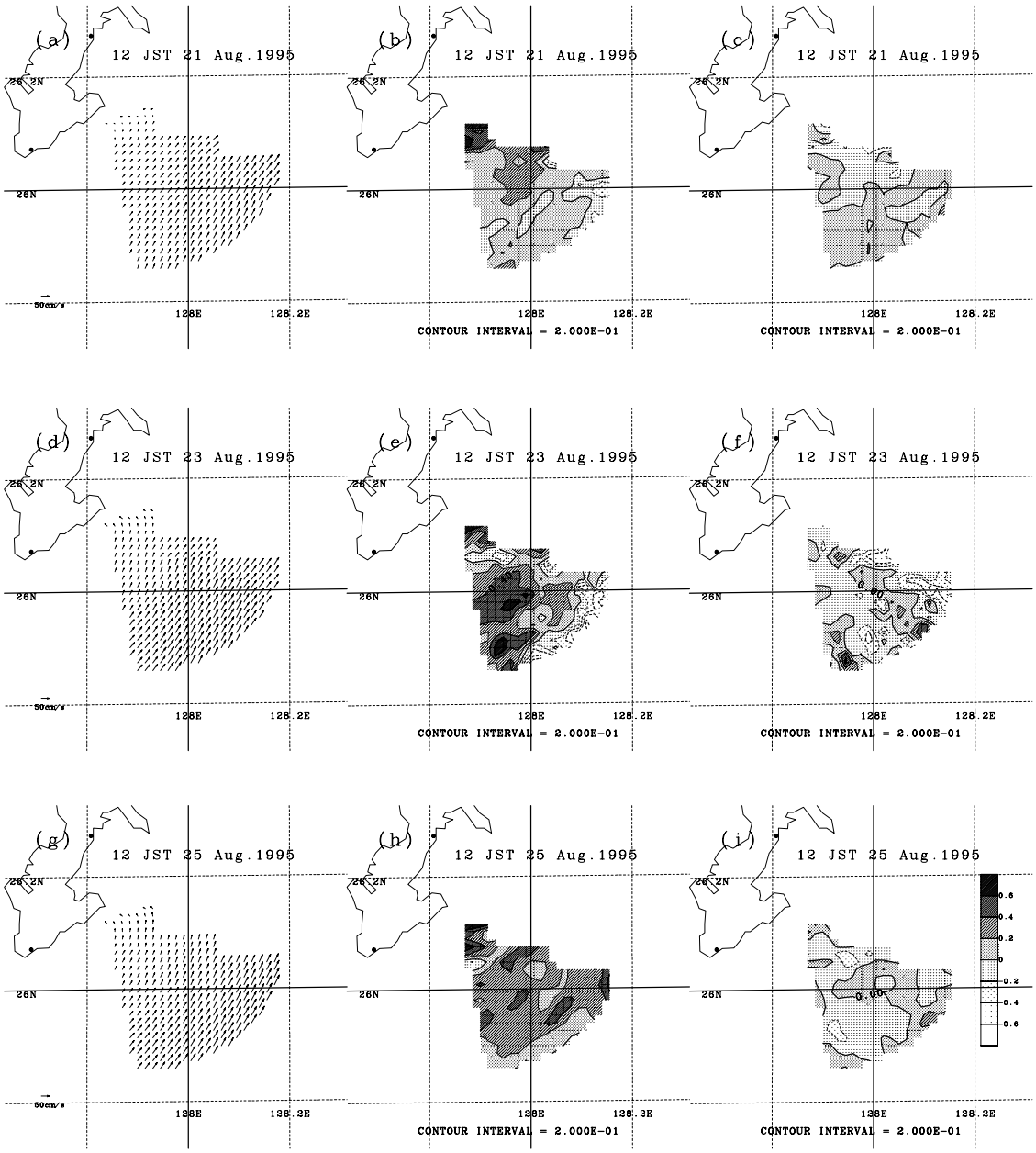

Figure 7. Low-frequency currents observed by HF ocean radars. (a) Current vector (1200 LT 21 August 1995), (b) relative vorticity (1200 LT 21 August 1995), (c) horizontal divergence (1200 LT 21 August 1995), (d) current vector (1200 LT 21 August 1995), (e) relative vorticity (1200 LT 21 August 1995), (f) horizontal divergence (1200 LT 21 August 1995), (g) current vector (1200 LT 21 August 1995), (h) relative vorticity (1200 LT 21 August 1995), and (i) horizontal divergence (1200 LT 21 August 1995). Relative vorticities and horizontal divergences are normalized by f.

piece lengths are approximately two local inertial periods. The horizontal wave number vector $\mathbf{k} = (k_x, k_y) = \nabla\phi$, where ∇ denotes horizontal gradient, was calculated by seeking the minimum of J as

$$J = \sum_{m,n} \left(k_x x_m + k_y y_n + d - \phi_{m,n}\right)^2, \tag{7}$$

where (m, n) is the grid number, and $\phi_{m,n}$ is the phase at position (x_m, y_n). The near-inertial current vector rotated clockwise, and the direction of $\mathbf{k} = \nabla\phi$ is the phase propagation direction. Variables k_x, k_y and d were estimated from measured currents in the HF-radar observation area.

[37] Figure 9 shows the horizontal distribution of near-inertial amplitudes A at 1200 LT from 21 to 26 August 1995. Amplitude A on 20 August 1995 could not be obtained. Near-inertial amplitudes were large on 21, 22, and 23 August, but they decreased from 24 August. The near-inertial amplitudes were small near the shore and large in the southeastern part of the HF-radar observation area, where the water depth is greater than 1000 m. This is in contrast to the measurements of *Chen et al.* [1996], who

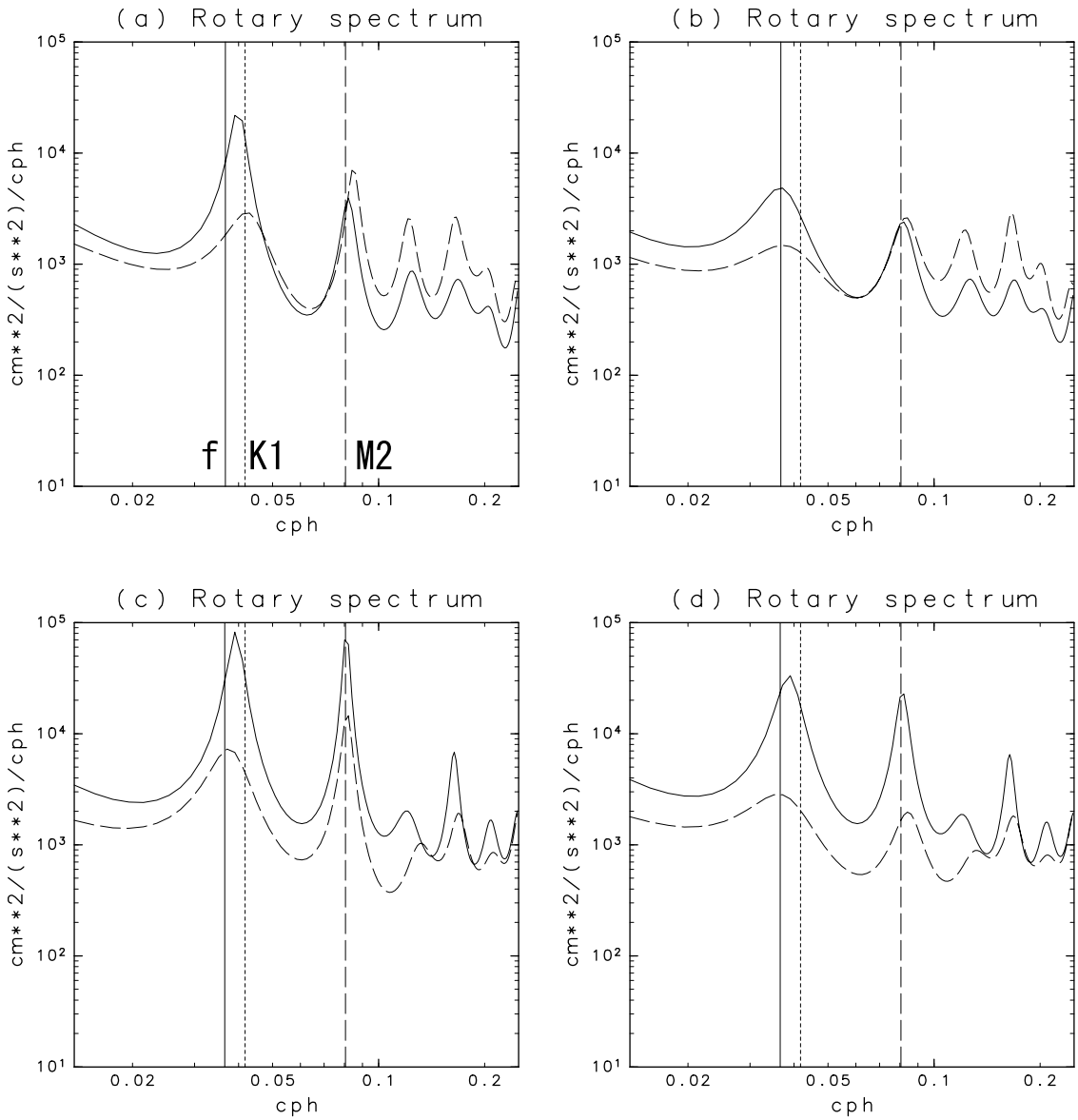

Figure 8. Rotary spectra of (a) HF radar observed currents at (26.059°N, 127.945°E), (b) detided currents at (26.059°N, 127.945°E), (c) HF radar observed currents at (25.951°N, 128.065°E), and (d) detided currents at (25.951°N, 128.065°E).

showed that a near-inertial amplitude was the largest in the shelf break and was reduced offshore.

[38] Figure 10 shows a time series of horizontal-wave directions and wavelengths of near-inertial currents. The near-inertial wave direction was southward until 23 August 1995, and turned to the northwestward on 23 August, while wind direction changed from southwestward to northwestward on 22 August (Figure 10b). Near-inertial wave directions were scattered after near-inertial amplitudes became small (on 25 August).

[39] The near-inertial wave direction was close to the wind direction (Figure 10b) when near-inertial oscillations were dominant. The near-inertial wavelength was on the order of 100 km until 23 August and on the order of 1000 km on 23 August. The near-inertial wavelength was long when the wave direction was northwestward. However, there were a few exceptions, when the near-inertial wavelength was the longest, and the error of the near-inertial wave number vector was sensitive to the error of phase. In contrast to the large spatial variability of near-inertial amplitudes A during the period, the spatial variability of the phase ϕ was small.

[40] The value of $IP \times U_t$ was close to the near-inertial wavelength until 24 August, when the typhoon was near the HF radar observation area. *Price* [1983] showed that along-storm track wavelength was $IP \times U_t$, and the cross-storm track scale is the storm scale. If the near-wave direction is northwestward (Figure 10a), the agreement of near-inertial wavelength with $IP \times U_t$ is consistent with *Price* [1983].

4. Slab Model

4.1. Formulation

[41] Horizontal gradients of the quasi-geostrophic flow in the background can affect the relationship between winds and surface currents. For example, *Weller et al.* [1991]

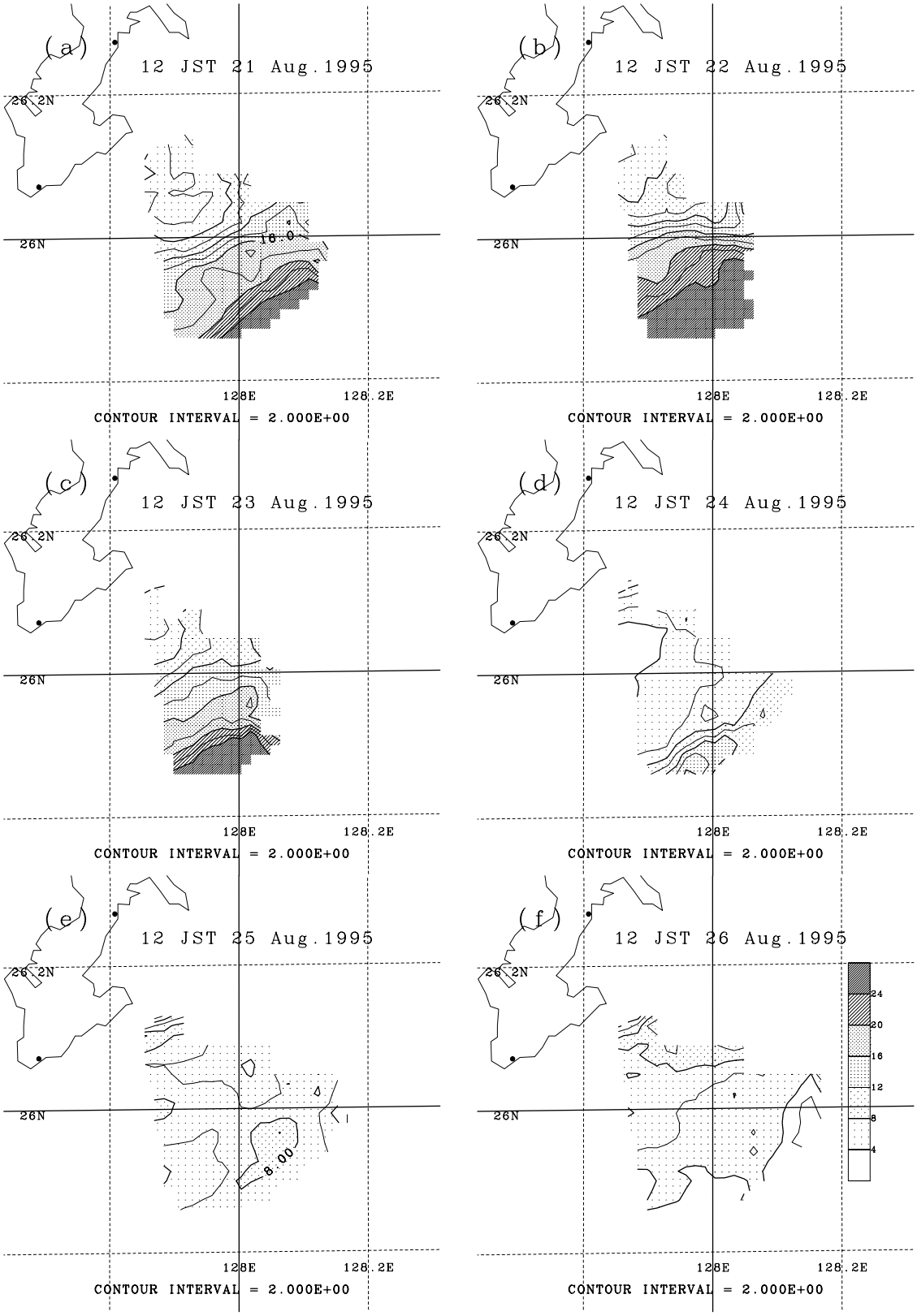

Figure 9. Horizontal distribution of near-inertial amplitude *A* estimated from HF radar observed currents at (a) 1200 LT 32 August 1995, (b) 1200 LT 22 August 1995, (c) 1200 LT 23 August 1995, (d) 1200 LT 24 August 1995, (e) 1200 LT 25 August 1995, and (f) 1200 LT 26 August 1995; unit: cm/s.

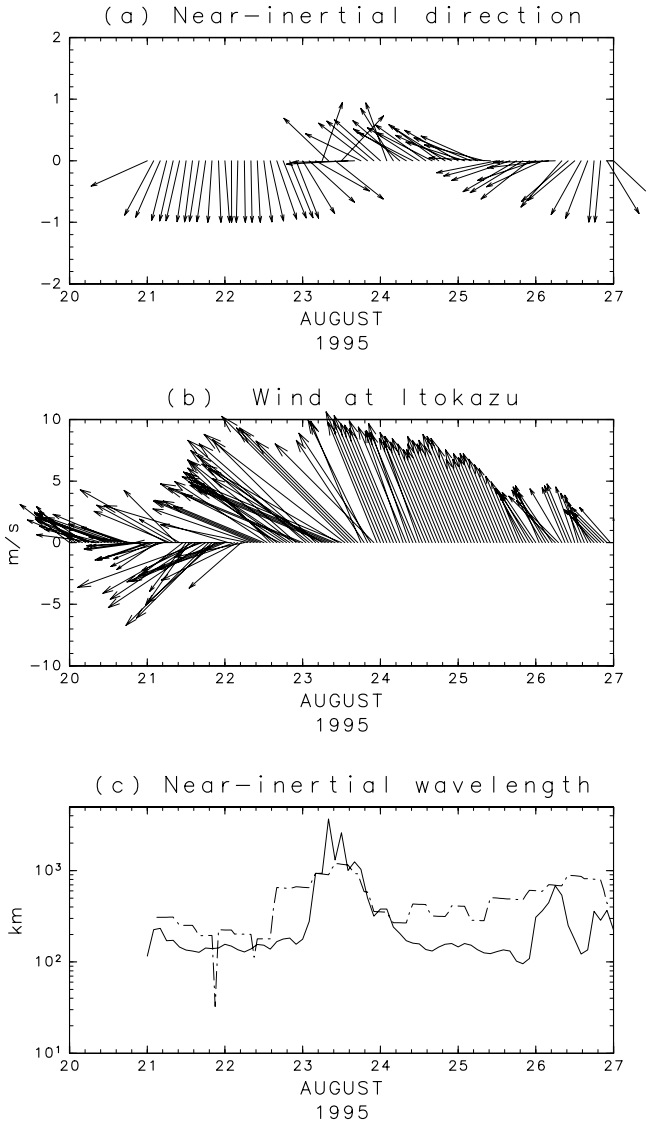

Figure 10. Time series of horizontal (a) wave directions (unit vectors) and (c) wavelengths (solid line) of near-inertial currents estimated from HF radar observed currents. Dashed line is $IP \times U_t$. (b) Wind vectors at Itokazu.

discussed the relationship and concluded that near-inertial oscillations are damped (amplified) with time when quasi-geostrophic currents are divergent (convergent).

[42] We used a simple slab model based on the equations

$$\frac{\partial u_m}{\partial t} + 2u_m\frac{\partial u_q}{\partial x} + u_m\frac{\partial v_q}{\partial y} + v_m\left(\frac{\partial u_q}{\partial y} - f\right) + U_a = \frac{\tau_x}{\rho H} - c_m u_m \tag{8}$$

$$\frac{\partial v_m}{\partial t} + 2v_m\frac{\partial v_q}{\partial y} + v_m\frac{\partial u_q}{\partial x} + u_m\left(\frac{\partial v_q}{\partial x} + f\right) + V_a = \frac{\tau_y}{\rho H} - c_m v_m, \tag{9}$$

where

$$U_a = 2u_q\frac{\partial u_m}{\partial x} + v_q\frac{\partial u_m}{\partial y} + u_q\frac{\partial v_m}{\partial y} \tag{10}$$

$$V_a = 2v_q\frac{\partial v_m}{\partial y} + u_q\frac{\partial v_m}{\partial x} + v_q\frac{\partial u_m}{\partial x}, \tag{11}$$

$\mathbf{x} = (x, y)$ is the horizontal coordinate, $\mathbf{u}_q = (u_q, v_q)$ is the quasi-geostrophic flow, $\mathbf{u}_m = (u_m, v_m)$ is the mixed layer velocity, H is the depth of the mixed layer of density ρ, τ_x and τ_y are the components of the wind stress vector, and c_m is a damping coefficient. This model is somewhat different from that of *Weller* [1982] and *Weller et al.* [1991]. The terms U_a and V_a are added to Weller's model. The Doppler shift of the near-inertial wave is considered by adding the terms U_a and V_a.

[43] There is a large difference between HF-ocean-radar derived currents and ocean mixed-layer currents in both magnitude and direction. The former currents are those at depth $\lambda_B/(4\pi)$ of 0.5 m, where λ_B is the Bragg wavelength [*Stewart and Joy*, 1974]. Our approach assumes that the HF-radar-derived surface currents reflect the mixed layer currents. The low-frequency current estimated in section 3 was used as a quasi-geostrophic current $\mathbf{u}_q = (u_q, v_q)$. The domain of the computation is only the area from which the low-frequency currents were estimated, and it is much smaller than the area affected by the typhoon.

[44] We considered two types of wind field models. One model is a uniform wind field model (UWFM), in which the wind field is uniform over the model domain. The wind vector of the UWFM ($\mathbf{V}_{UW}$) is the wind vector at Itokazu multiplied by a factor of 1.15, which was determined from the comparison of wind speeds at Itokazu and those given by TCWPM (equation (5)).

[45] The other model is a blended tropical-cyclone wind-profile model (BTCWPM), in which the TCWFM is blended into the UWFM. The wind vector of the BTCWPM (V_{BC}) is written as follows:

$$\mathbf{V}_{BC} = \mathbf{V}_{TC} + \frac{c^4}{1+c^4}\mathbf{V}_{bg}, \tag{12}$$

where $\mathbf{V}_{bg}$ is the background wind field [*Chu et al.*, 2000]. The background wind field was estimated as $\mathbf{V}_{bg} = \mathbf{V}_{UW} - \mathbf{V}_{TC}$.

[46] Figure 11, which is similar to Figure 3, shows the time series of wind vectors for the BTCWPM at 26°N and 128°E. This figure shows the clockwise rotation of the wind vector associated with the passage of the storm on 23 August, while the clockwise rotation cannot be seen clearly in Figure 3. The wind speeds given by the BTCWPM are larger than those given by the UWFM from 0900 LT 23 to 1700 LT 23 August. The wind speeds given by the UWFM are larger than those given by BTCWPM from 2100 LT 22 to 0800 LT 23 August, and from 1800 LT 23 to 1600 LT 24 August. The wind speeds given by the BTCWPM are the same as those given by the UWFM in other periods.

[47] The UWFM does not represent the wind field associated with a passage of the typhoon. However, the mixed layer current was simulated by using the UWFM to isolate the effect of quasi-geostrophic currents on the horizontal variability of near-inertial currents. Furthermore, the effect of the storm movement on near-inertial currents can be clarified by considering the UWFM.

[48] The mixed-layer-current vector, $\mathbf{u}_m$, was calculated by using both UWFM and BTCWPM. It was assumed $\mathbf{u}_m$

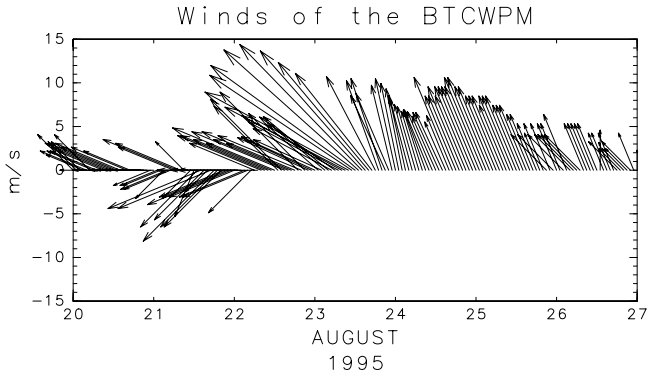

Figure 11. Time series of hourly winds of the BTCWPM at 26°N and 128°E.

was zero at 0600 LT 15 August 1995. The horizontal gradient of (u_m, v_m) in the upstream boundary was zero. The wind stress was calculated with the bulk formula of *Large and Pond* [1981]. Because there are unknown parameters in equations (8) and (9) such as H and c_m, we calculated mixed layer currents for various H and c_m to investigate the sensitivity of the predicted currents to these parameters. The parameters for calculations are H = 10, 20, 30, 40, and 50 m and c_m = 0.22 day^{-1} ($\simeq 1/(4IP)$) and c_m = 0.126 day^{-1} ($\simeq 1/(7IP)$).

[49] The multiplication factor 1.15 was fixed, because changing the value of the factor is almost equivalent to changing the parameter H. The time step was 1 min and the upstream scheme was adopted. Near-inertial amplitudes A, phase ϕ, and horizontal wave number vector **k** were estimated as stated in section 3 from calculated (u_m, v_m).

4.2. Results of a Numerical Computation in the Case of No Mesoscale Flows

[50] In the case of no mesoscale flows ($\mathbf{u}_q = (u_q, v_q) = \mathbf{0}$), equations (8) and (9) are written as

$$\frac{\partial U_m}{\partial t} + (if + c_m)U_m = \Gamma, \tag{13}$$

where $U_m = u_m + iv_m$ and $\Gamma = \Gamma(t) = (\tau_x + i\tau_y)/(\rho H)$. The solution of equation (13) is

$$U_m = U_{m0}\exp(-(if + c_m)t) + \int_0^t \exp(-(if + c_m)(t - t_1))\Gamma(t_1)dt_1, \tag{14}$$

where $U_{m0} = U_m$ at $t = 0$. If the wind stress rotates clockwise with a radian frequency f, i.e., $\Gamma(t) \propto \exp(-ift)$, and $c_m = 0$, equation (14) shows that the inertial amplitude is a linear function of time t. Figure 12a shows time series of observed near-inertial amplitudes and predicted near-inertial amplitudes from equation (14) for UWFM and BTCWPM at 26°N and 128°E. Observed near-inertial amplitudes are largest on 22 August, while predicted near-inertial amplitudes are largest on 24 August. The near-inertial amplitudes for the BTCWPM are much larger than those for the UWFM. We applied the complex demodulation (section 3) to the wind stress vectors at 26°N and 128°E for the UWFM and the BTCWPM. Figure 12b shows time series of clockwise rotation amplitudes at radian frequency f. The clockwise rotation amplitudes are large from 22 to 24 August. The magnitudes of the BTCWPM wind stress are larger than those of the UWFM wind stress from 0900 LT 23 to 1700 LT 23 August. The large inertial amplitudes of the BTCWPM wind stress are due to not only the large magnitudes of the BTCWPM wind stress but also due to the clockwise rotation of the BTCWPM winds associated with the storm movement.

[51] The near-inertial amplitudes are amplified with time (Figure 12a) from 22 to 24 August as expected from equation (14). Figure 12c shows the horizontal distribution of calculated near-inertial amplitudes for the BTCWPM at 1200 LT 23 August. The horizontal variability of near-inertial amplitudes was much smaller than that of observed near-inertial amplitudes (Figure 9c).

4.3. Results of the Numerical Computation for Uniform Wind Fields

[52] Figure 13 shows the horizontal distribution of near-inertial amplitudes calculated by the UWFM. The near-inertial amplitude was small in 1200 LT 21 August. The amplitudes became larger at 1200 LT 22 August (Figure 13b), but they were still smaller than those in Figure 9b. The amplitudes were larger at 1200 LT 23 August (Figure 13c), especially in the offshore area (as in Figure 9c), although the large-near-inertial amplitude area in Figure 9c was located in the southern part of the HF-radar observation area. The near-inertial amplitudes were still large at 1200 LT 24 August (Figure 13d), while the amplitudes became smaller in Figure 13d. The near-inertial currents decayed at 1200 LT 25 August (Figure 13e), but the horizontal variability was still large. The amplitudes were small at 1200 LT 26 August (Figure 13f), and the horizontal variability was not clear. In summary, as shown by the observed currents, the near-inertial amplitudes were the largest in the offshore area; however, there was a time lag of growth and decay between the observed and the predicted near-inertial currents.

[53] Figure 14 shows a time series of horizontal wave directions and wavelengths of calculated near-inertial currents. The near-inertial wave directions were also southward until 21 August 1995. The near-inertial wave vector rotated clockwise, and the direction was northeastward from 22 August to 26 August. The near-inertial wave directions were close to the wind directions shown in Figure 10.

[54] The near-inertial wavelength was on the order of 100 km, and the longest wavelength was about 1000 km when the predicted near-inertial amplitude was large. This result is consistent with the measured values (Figure 10c), although the calculated wavelengths were shorter than the measured ones. The near-inertial wavelengths agree with the value of with $IP \times U_t$ on 24 August when the predicted near-inertial amplitudes are large.

4.4. Sensitivity to Parameters

[55] Figure 15a shows the horizontal distribution of calculated near-inertial amplitudes at 1200 LT 23 August for H = 20 m and c_m = 0.22 day^{-1}. In the case of large H, predicted near-amplitudes are small; however, the horizontal distribution pattern of near-amplitudes is similar to that in Figure 13c. The near-amplitudes are large in the southeastern part of the HF-ocean-radar observation area. Figure 15b shows

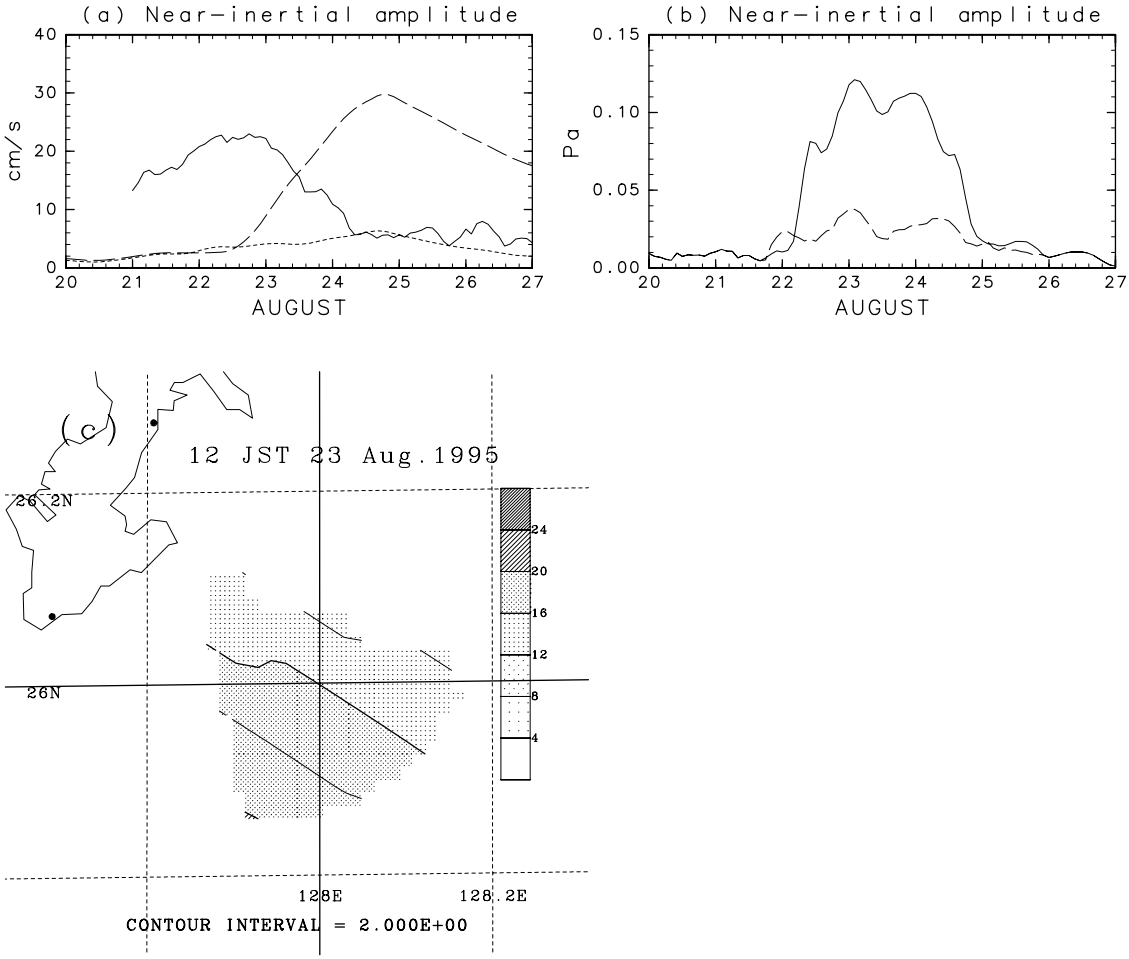

Figure 12. (a) Time series of observed near-inertial amplitudes (solid line) and predicted near-inertial amplitudes from equation (14) (no mesoscale flows) for UWFM (dotted line) and BTCWPM (dashed line) at 26°N and 128°E. (b) Time series of inertial amplitudes of wind stress of the BTCWPM (solid line) and the UWFM (dotted line). (c) Horizontal distribution of near-inertial amplitudes (A) estimated from predicted currents at 1200 LT 23 August 1995 from equation (14) for the BTCWPM. H = 50 m and c_m = 0.22 day^{-1} ($\simeq 1/(4IP)$).

the horizontal distribution of calculated near-inertial amplitudes at 1200 LT 25 August for H = 10 m and c_m = 0.126 day^{-1}. Figure 15b shows no significant differences from Figure 13e.

[56] Figures 15c and 15d show time series of horizontal near-inertial wave directions and wavelengths. There are no apparent differences between Figure 14 and Figures 15c and 15d. The near-inertial amplitude depends on H, but the horizontal distribution pattern of near-inertial amplitudes does not depend on H or c_m. The near-inertial wave phase also does not depend on H or c_m.

[57] To simulate mixed layer currents, the model was initialized with the inertial wave field at 0000 LT 21 August. The initial mixed layer currents $\mathbf{u}_m$ were estimated by extracting low-frequency currents and tidal currents from observed currents as explained in section 3. Figures 15e and 15f show near-inertial amplitudes at 1200 LT 24 August for the initial $\mathbf{u}_m$ and c_m of 0.22 day^{-1}. In the case of H = 10 m, the near-inertial amplitudes become larger; on the other hand, in the case of H = 50 m, the near-inertial amplitudes become smaller. This shows that the near-inertial waves vanish as the mixed layer deepens.

4.5. Spatial Variability of Wind Field

[58] Figure 16 shows the horizontal distribution of calculated near-inertial amplitudes for BTCWPM. The parameter H is 50 m, but near-inertial amplitudes are larger than those for the for UWFM (Figure 13). The wind speed for UWFM (Figure 13) is almost the same as that of the BTCWPM (Figure 16); there are significant differences in near-inertial amplitude. Because the wind vector of the TCWPM rotates clockwise in time and there is a near-resonance between wind-forcing vectors and near-inertial currents, the near-inertial amplitude becomes larger as shown Figure 16. The near-inertial amplitude was large near the shore (Figures 16b–16d). The effect of the island is not considered in the BTCWPM and the wind speed inferred from the BTCWPM is larger than the true wind speed. Therefore, the near-inertial amplitude was overestimated. The dependencies of near-inertial amplitudes on parameter H and c_m are the same as those for the UWFM.

[59] The BTCWPM was used to calculate mixed-layer currents (u_m, v_m). Figure 16 shows the horizontal distribution of calculated near-inertial amplitudes for calculated by the BTCWPM. Parameter H is 50 m, but near-inertial

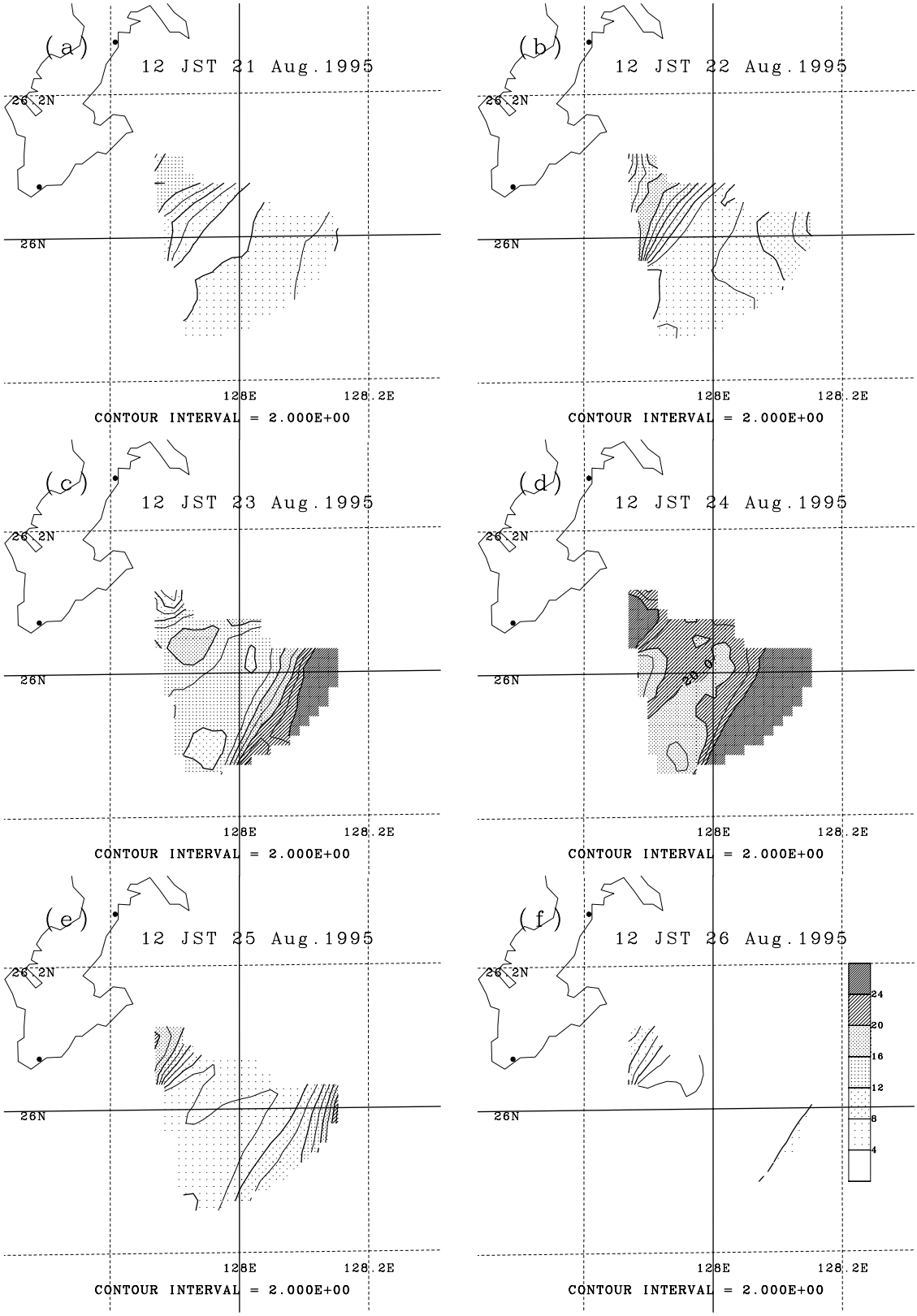

Figure 13. Same as Figure 9 but estimated from predicted currents for UWFM, H = 10 m and c_m = 0.22 day^{-1} ($\simeq 1/(4IP)$).

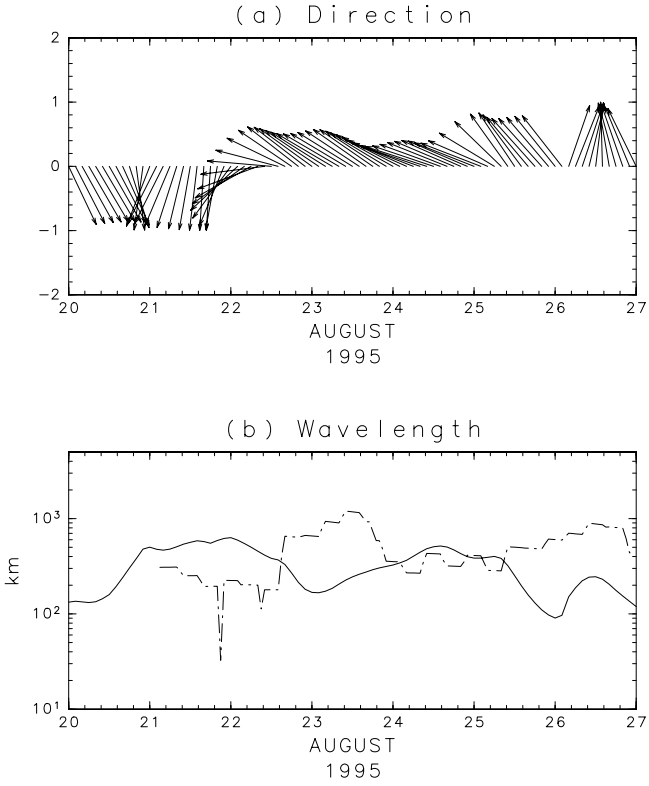

Figure 14. Same as Figure 10 but estimated from predicted currents for UWFM, H = 10 m and c_m = 0.22 day^{-1} ($\simeq 1/(4IP)$).

amplitudes are larger than those given by the UWFM (Figure 13). The wind speed determined by the UWFM (Figure 13) is almost the same as that given by the BTCWPM (Figure 16), but there are significant differences in near-inertial amplitude. Because the wind vector given by the TCWPM rotates clockwise in time and there is a near-resonance between wind-forcing vectors and near-inertial currents, the near-inertial amplitude becomes larger (as shown in Figure 16). The near-inertial amplitude was large near the shore (Figures 16b–16d). The effect of the island is not considered in the BTCWPM, and the wind speed inferred from the BTCWPM is larger than the true wind speed. The near-inertial amplitude was therefore overestimated. The dependencies of near-inertial amplitudes on parameters H and c_m are the same as those given by the UWFM (section 4.4).

[60] Figure 17 shows a time series of horizontal wave directions and wavelengths of calculated near-inertial currents given by the BTCWPM. Note that Figure 17 is similar to Figure 14. However, one difference is that the near-inertial wave direction is almost westward or southwestward on 22 August in Figure 17a, while it is westward or northwestward on 22 August in Figure 14a. This difference in direction is due to the movement of the typhoon. The clockwise angle from vector $\mathbf{U}_t$ to vector $\mathbf{r}$ is larger in the eastern part of the HF-radar observation area than that in the western part (Figure 2), and the phase ϕ is more advanced in the eastern part. The direction of the vector $\mathbf{k} = \nabla\phi$ was therefore westward. The other difference is that the maximum wavelength occurs on 24 August in Figure 14b, but it occurs on 22 August in Figure 17b, which is the transition period from the uniform wind field to the TCWPM in the BTCWPM. The horizontal distribution of near-inertial phase ϕ is complicated by the combined effect of the horizontal variability of the winds and mesoscale currents. As a result, estimated wave number $k = |\mathbf{k}|$ is small in this period. The agreement of the near-inertial wavelengths with $IP \times U_t$ is also good on 24 August, when the predicted near-inertial amplitudes are large.

5. Discussion

5.1. Dispersion Relation

[61] The spatial variability of near-inertial amplitude A is discussed in terms of the dispersion relation derived from equations (8) and (9). It is assumed that near-inertial wave variables can be written in the form of a plane wave that is proportional to $\exp(i(\mathbf{k}\cdot\mathbf{x} - \omega t))$, where $\omega = \omega_r + i\omega_i$ is the complex frequency, ω_r is the real part, and ω_i is the imaginary part. It is also assumed that u_q, v_q, $\partial u_q/\partial x$, $\partial u_q/\partial y$, $\partial v_q/\partial x$, and $\partial v_q/\partial y$ are constants. The right-hand side of equations (8) and (9) are considered to be zero (τ_x, τ_y = 0, c_m = 0) here. If $|\partial u_q/\partial x|$, $|\partial u_q/\partial y|$, $|\partial v_q/\partial x|$, $|\partial v_q/\partial y| \ll f$ [*Kunze*, 1985],

$$\omega_r \simeq \mathbf{k}\cdot\mathbf{u}_q \pm \left[f + \frac{1}{2}\left(\frac{\partial v_q}{\partial x} - \frac{\partial u_q}{\partial y}\right)\right] \tag{15}$$

and [*Weller*, 1982]

$$\omega_i \simeq -\frac{1}{2}\left(\frac{\partial u_q}{\partial x} + \frac{\partial v_q}{\partial y}\right) \tag{16}$$

are obtained. Equation (16) shows that near-inertial oscillations are damped (amplified) with time when quasi-geostrophic currents are divergent (convergent). Near-inertial amplitudes (Figures 9 and 13) are likely to be related to the divergence of low-frequency currents (Figure 7).

[62] Equations (8) and (9) can be written in terms of $U_m = u_m + iv_m$. If it is assumed that $U_m \propto \exp(i(\mathbf{k}\cdot\mathbf{x} - \omega t))$, the auxiliary equation for ω can be obtained as

$$\begin{aligned}&\omega^2 + 3\left[i\left(\frac{\partial u_q}{\partial x} + \frac{\partial v_q}{\partial y}\right) - \mathbf{k}\cdot\mathbf{u}_q\right]\omega \\ &- \left[2\frac{\partial u_q}{\partial x} + \frac{\partial v_q}{\partial y} + i\left(\mathbf{k}\cdot\mathbf{u}_q + k_x u_q\right)\right]\left[2\frac{\partial v_q}{\partial y} + \frac{\partial u_q}{\partial x} + i\left(\mathbf{k}\cdot\mathbf{u}_q + k_y v_q\right)\right] \\ &+ \left(\frac{\partial u_q}{\partial y} - f + ik_y u_q\right)\left(\frac{\partial v_q}{\partial x} + f + ik_x v_q\right) = 0.\end{aligned} \tag{17}$$

Thus ω can be calculated from $\mathbf{u}_q$ and $\mathbf{k}$ by solving equation (17).

[63] Figure 18 shows contour maps of ω_i/f for $\omega_r < 0$, where $\omega = \omega_r + i\omega_i$ is the solution of equation (17). The horizontal wave number vector $\mathbf{k}$ is estimated from predicted currents (Figure 14). Positive (negative) ω_i indicates an amplification (decay) of near-inertial amplitude A with time. The value of ω_i indicates the growth rate of the inertial wave.

[64] The value of ω_i of *Weller* [1982] (equation (16)) is about $\pm 0.1f$ from Figure 7, so the value of ω_i in Figure 18 is larger than that given by equation (16). The value of ω_i is small in Figure 18a, and the predicted near-inertial

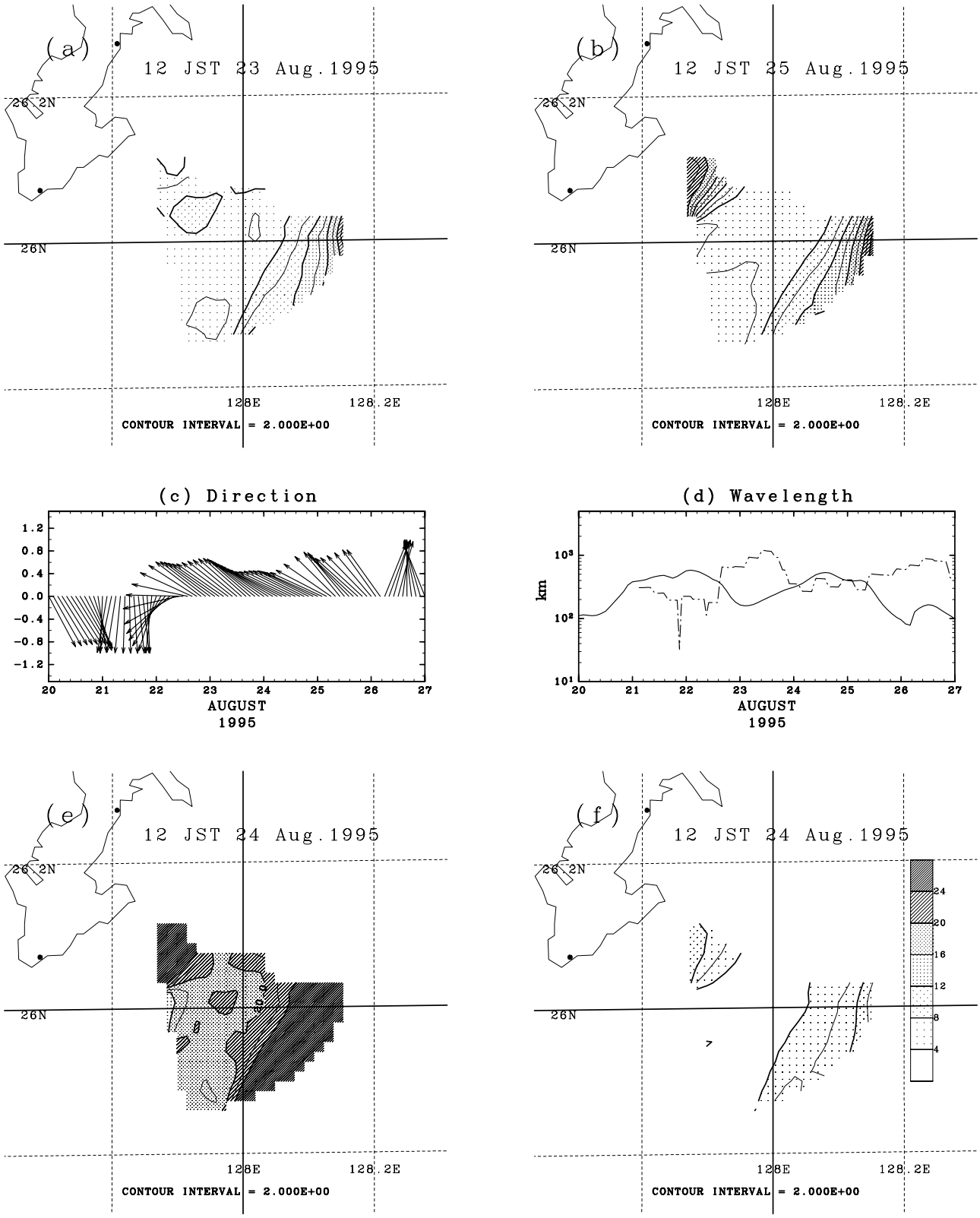

Figure 15. Horizontal distribution of near-inertial amplitudes (A) estimated from predicted currents ((a) 1200 LT 23 August for the UWFM, $H = 20$ m and $c_m = 0.22$ day^{-1}, and (b) 1200 LT 25 August for the UWFM, $H = 10$ m, $c_m = 0.126$ day^{-1}), and time series of horizontal (c) wave directions (unit vectors) and (d) wavelengths (solid line) of near-inertial waves estimated from predicted currents for $H = 30$ m and $c_m = 0.126$ day^{-1}. Dashed line represents $IP \times U_t$. (e) Same as Figure 15a but at 1200 LT 24 August and for $H = 10$ m. Mixed-layer current $\mathbf{u}_m$ is initialized with the inertial wave field on 0000 LT 21 August. (f) Same as Figure 15e but for $H = 50$ m.

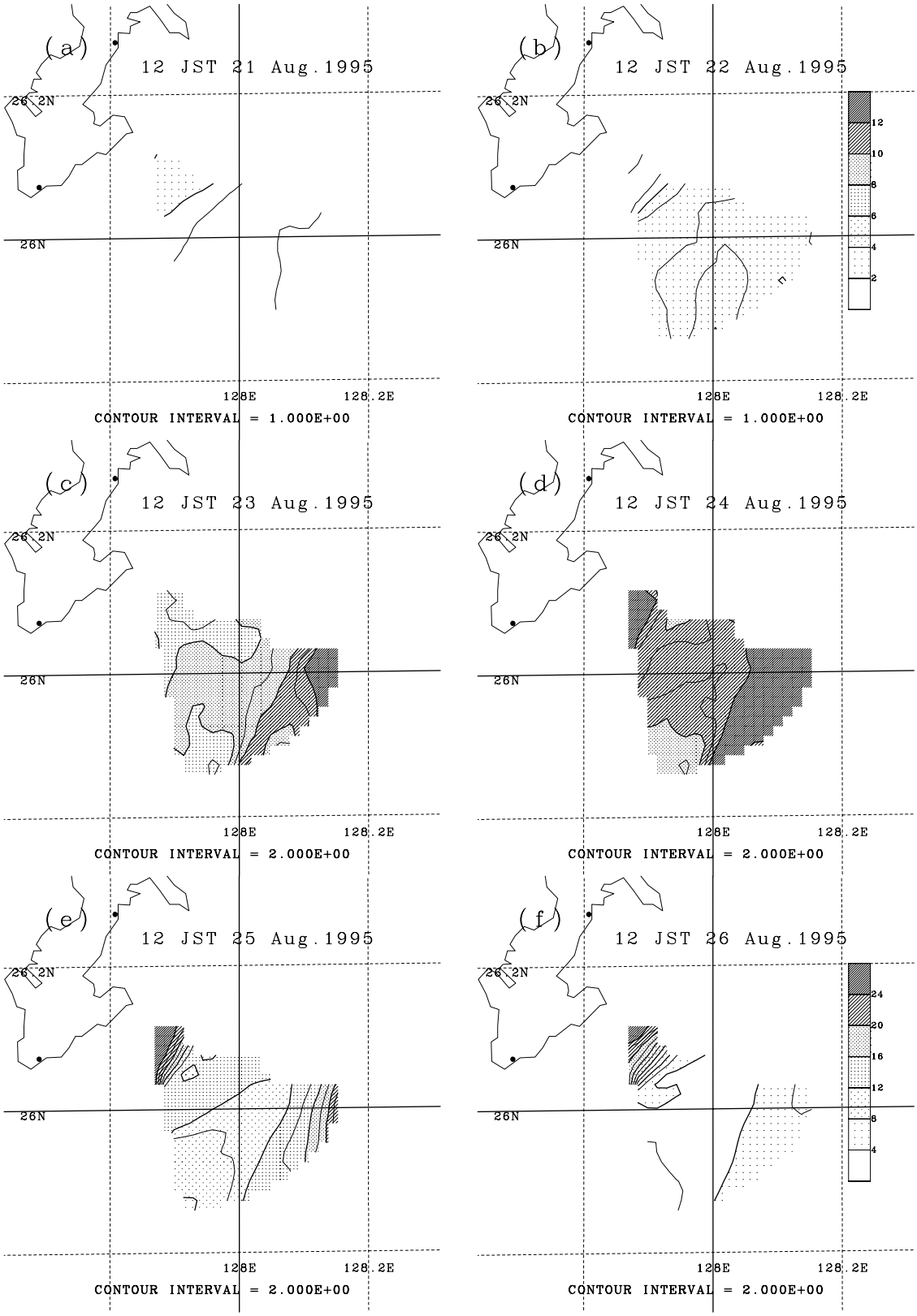

Figure 16. Same as Figure 13 but for BTCWPM and H = 50 m.

amplitude is also was small at that time (Figure 13a). The value of ω_i became larger at 1200 LT 22 August (Figure 18b). This value was the largest in the northwestern part and the eastern part of the HF-radar observation area in Figure 18b. This result is consistent with Figure 13b, but the near-inertial amplitude in the northwestern part is small in Figure 9b. The value of ω_i became even larger at 1200 LT 23 August (Figure 18c). In this figure, the growth rate was the largest in

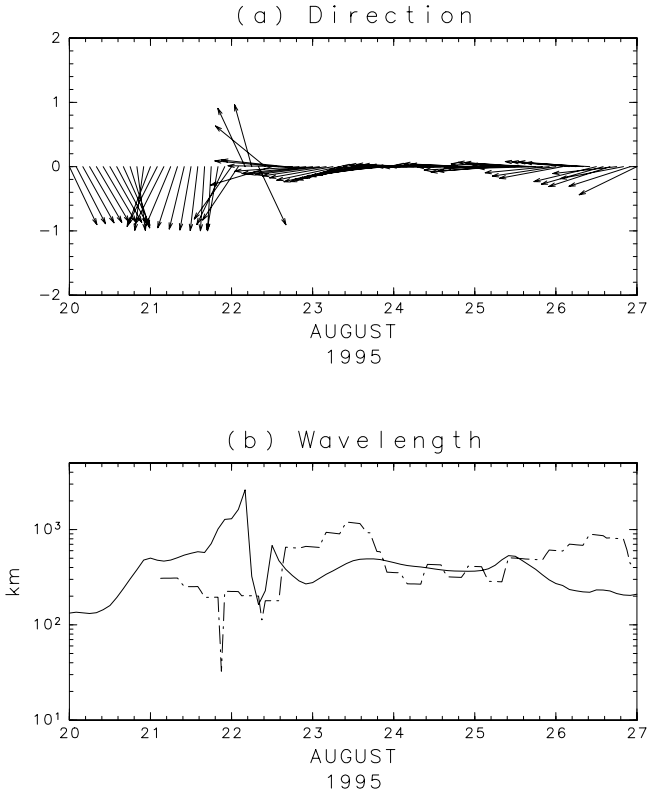

Figure 17. Same as Figure 14 but estimated from predicted currents for BTCWPM and H = 50 m.

the eastern part of the HF-radar observation area in Figure 18c, where the predicted near-inertial amplitude was the largest (Figure 13c).

[65] The value of ω_i became smaller at 1200 LT 24 August (Figure 18d). However, the growth rate was the largest in the eastern part of the HF radar observation area in Figure 18d. Thus the growth rate was related to the horizontal distribution of near-inertial amplitudes.

[66] The value of ω_i was the largest in the eastern part of the observation area. It seems to be the largest on 21 August in this example. This result shows that the near-inertial amplitude grew on that day. In some cases, the near-inertial amplitude was small even if the value of ω_i was large. The wind stress was also small in these cases. The wind stress and the value of ω_i are important for interpreting spatial and temporal variability of near-inertial oscillations.

5.2. Comparison Between Observed and Predicted Near-Inertial Oscillations

[67] The discrepancies in near-inertial amplitudes are those of temporal variation and spatial variation. As an example of temporal variation, near-inertial amplitudes were large on 22 August and small on 24 August for the observed currents. On the other hand, near-inertial amplitudes were small on 22 August and large on 24 August for the predicted currents.

[68] The first possible explanation of the discrepancy is the temporal variations of the mixed-layer depth H. Depth H was shallow until 22 August, and deepened from 23 August. The transition speed of the typhoon reduced from 24 August. The entrainment is significant under slowly moving tropical cyclones [*Price*, 1983], and the mixed-layer depth H was increased. The discrepancies on 23 August (Figures 13b and 16b) and on 25 August (Figures 13b and 16b) can be explained by the temporal variations of mixed-layer depth H. A second possible explanation of the discrepancy is that the wind stress is not realistic both in the BTCWMP and the UWFM. The wind direction was changed significantly, and temporal variation of winds was complicated from 21 to 22 August (Figure 3), which suggests that spatial variability of the wind field was also complicated. A third possible explanation is the error of the estimated low-frequency currents. The HF-ocean current data were not available from 18 August to 19 August (section 2.1), and the error of the low-frequency currents inferred from the interpolation is large. These results thus mean that the near-inertial amplitude is sensitive to the low-frequency currents (Figure 13).

[69] The spatial discrepancy between the predicted and observed near-inertial amplitudes shows that the near-inertial amplitudes estimated from the observed currents were large in the southern part of the observation area, whereas the near-inertial amplitudes estimated from the predicted currents were large in the southeastern part. This discrepancy may be due to the small area of the computation, or the effect of the boundary condition. The other discrepancy in the spatial variability of near-inertial amplitude is that the near-inertial amplitudes of predicted currents were large near the coast (Figure 16). This discrepancy is not significant in the case of the UWFM (Figure 13). However, in the case of the BTCWPM, it is due to the overestimation of wind speeds.

[70] The near-inertial wave direction of the observed currents changed to northwestward from southward on 23 August. However, the direction estimated from predicted currents changed from southward to northwestward in the case of the UWFM (Figure 10a) or westward in the case of BTCWPM (Figure 17a). Because the scale of the computation domain is much smaller than the horizontal wavelength, the wave number vector is sensitive to the error of phase ϕ. Therefore the wave number vector estimated from the predicted currents does not agree with the wave number vector estimated from the observed currents.

6. Conclusions

[71] The horizontal spatial variability of near-inertial currents associated with a passage of a typhoon (tropical storm) was investigated by means of HF ocean radars. This investigation showed that the near-inertial amplitude was large in the offshore area and small near the coast. Moreover, the phase-propagation direction was close to the wind direction when the near-inertial oscillation was dominant. The order of the maximum near-inertial wavelength was 1000 km when the near-inertial amplitude was the largest. In addition, the near-inertial wavelength was close to the product of the inertial period and the storm translation speed.

[72] A slab model, which incorporates low-frequency currents, was used to calculate near-inertial currents. In the model, the near-inertial amplitude was large in the offshore area but small near the coast. The phase-propagation direction was also close to the wind direction in the model for the UWFM, and the maximum near-inertial

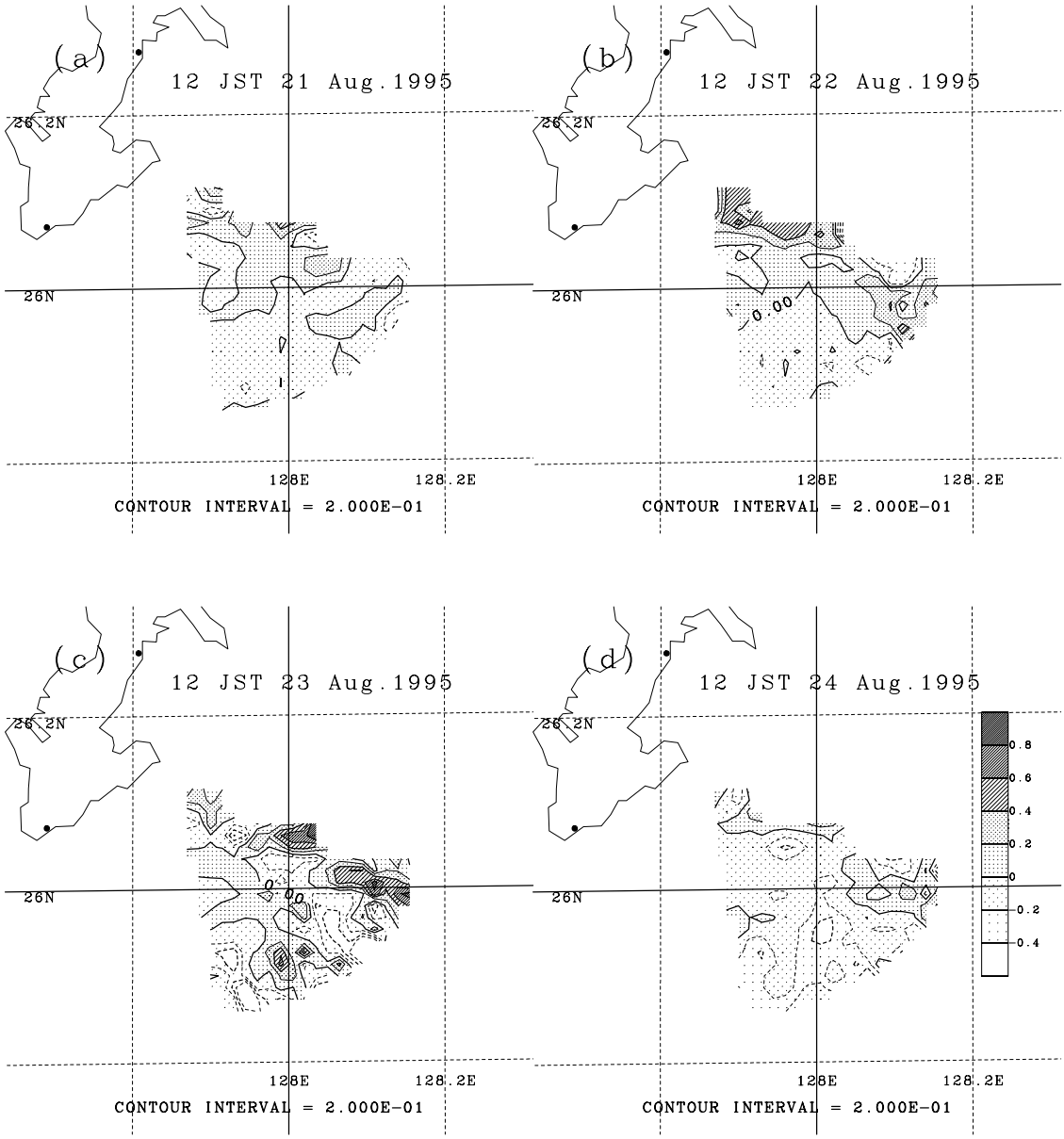

Figure 18. Contour maps of ω_i/f for $\omega_r < 0$ estimated from predicted currents at (a) 1200 LT 21 August 1995, (b) 1200 LT 22 August 1995, (c) 1200 LT 23 August 1995, and (d) 1200 LT 24 August 1995.

horizontal wavelength was on the order of 1000 km. The near-inertial wavelength was also close to $IP \times U_t$ when the near-inertial oscillation was large.

[73] The spatial and temporal variability of near-inertial oscillations were interpreted according to a dispersion relation derived from the slab model. A positive (negative) value of ω_i, which is the imaginary part of the solution of equation (17), indicates the growth (decay) of near-inertial oscillations. This value was large in the offshore area, which indicates the growth ratio of near-inertial oscillations was large. The possible reasons for the discrepancy between the observed and predicted near-inertial currents were temporal and spatial variability of the mixed-layer depth, errors of wind stress and mesoscale currents, and the small area of the simulation.

[74] The propagation of near-inertial waves cannot be considered because of the small area of the simulation. Accordingly, the authors should calculate near-inertial currents in a large domain. Such application of the model to a large area is the next subject of study.

[75] **Acknowledgments.** The authors acknowledge the anonymous reviewers for their insightful comments on the manuscript. The authors acknowledge the staff of the Okinawa Radio Observatory, Communications Research Laboratory for providing the Doppler spectrum data measured by the HF ocean radars. The authors acknowledge the Japan Meteorological Agency for providing the meteorological data. The GFD-DENNOU Library (http://dennou.gaia.h.kyoto-u.ac.jp/arch/dcl/) was used for drawing the figures.

References

AVISO, Sea level anomalies, in AVISO user handbook for sea level anomalies, ed. 3.1, *AVI-NT-011-312-CN*, 24 pp., Collecte Local. Satell., Space Oceanogr. Div., Toulouse, France, 1998.

Brink, K. H., Observations of the response of thermocline currents to a hurricane, *J. Phys. Oceanogr.*, *19*, 1017–1022, 1989.

Carr, L. E., and R. L. Elsberry, Models of tropical cyclone wind distribution and beta-effect propagation for application to tropical cyclone track forecasting, *Mon. Weather Rev.*, *125*, 3193–3209, 1997.

Chant, R. J., Evolution of near-inertial waves during an upwelling event on the New Jersey inner shelf, *J. Phys. Oceanogr.*, *31*, 746–764, 2001.

Chen, C., R. O. Reid, and W. D. Nowlin Jr., Near-inertial oscillations over the Texas-Louisiana shelf, *J. Geophys. Res.*, *101*, 3509–3524, 1996.

Chu, P. C., J. M. Veneziano, C. Fan, M. J. Carron, and W. T. Liu, Response of the South China Sea to tropical cyclone Ernie 1996, *J. Geophys. Res.*, *105*, 13,991–14,009, 1996.

D'Asaro, E. A., Upper-ocean inertial currents forced by a strong storm: II. Modeling, *J. Phys. Oceanogr.*, *25*, 2937–2952, 1995.

Dvorak, V. F., Tropical cyclone intensity analysis and forecasting from the satellite imagery, *Mon. Weather Rev.*, *103*, 420–430, 1975.

Emery, W. J., and R. E. Thompson, Time-series analysis methods, in *Data Analysis Methods in Physical Oceanography*, pp. 371–567, Pergamon Press, New York, 1998.

Etro, J. F., and J. P. Bassi, 1995 annual tropical cyclone report, 289 pp., U. S. Nav. Pac. Meteorol. Oceanogr. Cent. West, Joint Typhoon Warning Cent., Guam, Mariana Islands, 1995.

Hagiwara, T., S. Osano, S. Akashi, H. Koba, and T. Harada, Regression analysis to estimate gale-force and storm-force area of a typhoon using parameters extracted from GMS imagies (in Japanese), *J. Meteorol. Res.*, *41*, 89–99, 1989.

Hisaki, Y., Nonlinear inversion of the integral equation to estimate ocean wave spectra from HF radar, *Radio Sci.*, *31*, 25–39, 1996.

Hisaki, Y., Short-wave directional properties in the vicinity of atmospheric and oceanic fronts, *J. Geophys. Res.*, *107*(C11), 3188, doi:10.1029/2001JC000912, 2002.

Hisaki, Y., Short-wave directional distribution for first-order Bragg echoes of the HF ocean radars, *J. Atmos. Oceanic Technol.*, in press, 2003.

Hisaki, Y., W. Fujiie, T. Tokeshi, K. Sato, and S. Fujii, Surface current variability east of Okinawa Island obtained from remotely sensed and in situ observational data, *J. Geophys. Res.*, *106*, 31,057–31,073, 2001.

Holland, G. J., An analytic model of the wind and pressure profiles in hurricanes, *Mon. Weather Rev.*, *108*, 1212–1218, 1980.

Kunze, E., Near-inertial wave propagation in geostrophic shear, *J. Phys. Oceanogr.*, *15*, 544–565, 1985.

Large, W. G., and S. Pond, Open ocean momentum flux measurements in moderate to strong winds, *J. Phys. Oceanogr.*, *11*, 324–336, 1981.

Peters, H., L. K. Shay, A. J. Mariano, and T. M. Cook, Current variability on a narrow shelf with large ambient vorticity, *J. Geophys. Res.*, *107*(C8), 3087, doi:10.1029/2001JC000813, 2002.

Price, J. F., Upper ocean response to a hurricane, *J. Phys. Oceanogr.*, *11*, 153–175, 1981.

Price, J. F., Internal wave wake of a moving storm: I. Scales, energy budget and observations, *J. Phys. Oceanogr.*, *13*, 949–965, 1983.

Price, J. F., T. B. Sanford, and G. Z. Forristall, Forced stage response to a moving hurricane, *J. Phys. Oceanogr.*, *24*, 233–259, 1994.

Shay, L. K., H. C. Graber, D. B. Ross, and R. D. Chapman, Mesoscale surface current structure detected by HF radar, *J. Atmos. Oceanic Technol.*, *12*, 881–900, 1995.

Shay, L. K., A. J. Mariano, S. D. Jacob, and E. Ryan, Mean and near-inertial ocean current response to hurricane Gilbert, *J. Phys. Oceanogr.*, *28*, 858–889, 1998a.

Shay, L. K., T. N. Lee, E. J. Williams, H. G. Graber, and C. G. H. Rooth, Effects of low-frequency current variability on near-inertial submesoscale vortices, *J. Geophys. Res.*, *103*, 18,691–18,714, 1998b.

Shay, L. K., S. J. Lentz, H. C. Graber, and B. K. Haus, Current structure variations detected by HF radar and vector measuring current meters, *J. Atmos. Oceanic Technol.*, *15*, 237–256, 1998c.

Stewart, R. H., and J. W. Joy, HF radio measurements of surface currents, *Deep Sea Res.*, *21*, 1039–1049, 1974.

Takeoka, H., Y. Tanaka, Y. Ohno, Y. Hisaki, A. Nadai, and H. Kuroiwa, Observation of the Kyucho in the Bungo Channel by HF radar, *J. Oceanogr.*, *51*, 699–711, 1995.

van Meurs, P., Interactions between near-inertial mixed layer currents and the mesoscale: The importance of spatial variabilites in the vorticity field, *J. Phys. Oceanogr.*, *28*, 1363–1388, 1998.

Weller, R. A., The relation of near-inertial motions observed in the mixed layer during the JASIN (1978) experiment to the local wind stress and to the quasi-geostrophic flow field, *J. Phys. Oceanogr.*, *12*, 1122–1136, 1982.

Weller, R. A., D. L. Rudnick, C. C. Eriksen, K. L. Polzin, N. S. Oakey, J. W. Toole, R. W. Schmitt, and R. T. Pollard, Forced ocean response during the frontal air-sea interaction experiment, *J. Geophys. Res.*, *96*, 8611–8638, 1991.

Young, W. R., and M. Ben Jelloul, Propagation of near-inertial oscillations through a geostrophic flow, *J. Mar. Res.*, *55*, 735–766, 1997.

Zedler, S. E., T. D. Dickey, S. C. Doney, J. F. Price, X. Yu, and G. L. Mellor, Analyses and simulations of the upper ocean's response to Hurricane Felix at the Bermuda Testbed Mooring site: 13–23 August 1995, *J. Geophys. Res.*, *107*(C12), 3232, doi:10.1029/2001JC000969, 2002.

Y. Hisaki, Department of Physics and Earth Sciences, Faculty of Science, University of the Ryukyus, 1 Aza-Senbaru, Nishihara-cho, Nagasaki-gun, Okinawa 903-0213, Japan. (hisaki@sci.u-ryukyu.ac.jp)

T. Naruke, Metocean Environment Inc., 2-2-2 Hayabuchi, Tsuzuki-ku, Yokohama 224-0052, Japan. (ntatsuno@notes.metocean.co.jp)